Title
Using calcium imaging to understand function and learning in layer 2/3 of cerebral cortex

Author
Clancy, Kelly

Publication Date
2014

Peer reviewed|Thesis/dissertation

Using calcium imaging to understand function and learning in layer 2/3 of cerebral cortex

by

Kelly Bryn Clancy

A dissertation submitted in partial satisfaction of the
requirements for the degree of

Doctor of Philosophy

in

Biophysics

in the

Graduate Division

of the University of California, Berkeley

Committee in charge:

Prof. Daniel E. Feldman, Chair
Prof. Michael DeWeese
Prof. Yang Dan
Prof. Jon Wallis

Spring 2014

ABSTRACT

Using calcium imaging to understand function and learning in layer 2/3 of cerebral cortex

by

Kelly Bryn Clancy

Doctor of Philosophy in Biophysics

University of California, Berkeley 2014

Professor Daniel Feldman, Chair

Sensory information is encoded with sparse spiking in rodent sensory cortex, but the organization and functional basis of this sparse code is not well understood. I conducted two studies to characterize function and learning in the cortex. In the first study, I used population calcium imaging to study the circuit-level factors underlying sparse coding in layer (L) 2 of mouse somatosensory cortex. Whisker deflection elicited low-probability spikes in small, shifting neural ensembles spanning multiple cortical columns. Neurons within a column-sized imaging field were tuned heterogeneously to many different whiskers, contrary to standard models of somatotopy. A spectrum of whisker-evoked response probability existed across neurons that correlated strongly with spontaneous firing rate. This correlation indicates that a major component of responsiveness is independent of experimental stimulus choice. The distribution of responsivity was skewed, indicating the existence of a small population of highly-responsive neurons. Highly-responsive neurons included pyramidal cells and interneurons, and individual whisker deflections were primarily encoded by a small, stable population of highly responsive cells. L2 neurons projecting to motor (M1) and secondary somatosensory (S2) cortex differed in whisker tuning and sparseness, suggesting these intermingled populations send disparate information to their targets. Thus, sparse coding in L2 reflects heterogeneous sensory tuning, low average response probability across neurons, a skewed distribution of inherent responsiveness that includes a small number of more-active neurons, and functional specialization of S1 output streams.

In order to test whether the large pool of unresponsive neurons observed might be important in learning, I developed a novel type of brain-machine interface (BMI) based on calcium imaging in the intact cortex. In this BMI task, the mouse learned to use voluntary modulations of neural activity to control a device. The BMI design allowed for direct control over the relationship between neuronal activity and behavioral output. We trained mice to operantly control an auditory cursor using spike-related calcium signals recorded with 2-photon imaging in motor and somatosensory cortex. Mice rapidly learned to modulate activity in layer 2/3 neurons, evident both across- and within-sessions. Learning was accompanied by striking modifications of firing correlations within spatially localized networks at fine scales (10-100 microns). We found that less-active neurons, and even silent neurons, could dramatically up-modulate their firing to successfully learn the task. Neurons in a 'cloud' around the BMI-controlling neurons initially exhibited task-related activity, which dampened out as the animal honed in on the specific cells controlling the device. This suggests an economization of activity, which may be reflective of the sparse firing strategies in the cortex.

These studies both point to the existence of a gradient of activity in cortical neurons in L2/3, which can nevertheless be volitionally manipulated by learning. Neurons in L2/3 of rodent somatosensory cortex had unexpectedly divergent tuning, organized in a salt-and-pepper

fashion. The reliability of their responses depended mainly on intrinsic, stimulus-independent responsivity, and more minimally on tuning and downstream targets. However, even extremely inactive neurons could be induced to modify their firing dramatically by coupling their activity to reward. The network rapidly learned to minimize the number of neurons necessary to perform the task, suggesting that an economizing impetus might be at work in superficial cortex.

For my parents

Table of Contents

List of Figures
Chapter I

Chapter II

ACKNOWLEDGEMENTS

Thanks to Dan Feldman for being such a wonderful mentor and teacher over the years: for pressing me to ask the most important questions as carefully as possible, for being a constant source of encouragement and motivation throughout even the inevitably dark days of graduate school. His fairness, openness and insightfulness will serve as a model for all my future work. If I manage to pose a single question as well as Dan, I will consider myself a successful scientist. Thanks also to my previous mentor, the late physicist Jim Elliot, for being one of the most caring people I met at MIT, and for providing a different experience of science than I'd previously known. If it were not for him, I would have left science years ago and never looked back. Thanks to my committee members Mike DeWeese, Yang Dan and Jon Wallis for their encouraging and helpful guidance regarding my projects over the years. Their work has inspired me. I will never forget Mike's enthusiasm, nor his stories about crazy physicists. Thanks to Marla Feller for her wise advice, and my gratitude and respect go to both Yang and Marla for being such incredible role models for women in science, something I had lacked before coming to Berkeley. Thanks to Aaron Koralek for working on the CaBMI project with me, and being so much fun to work with. Thanks also go to Jose Carmena and Rui Costa for their great input on this project. Special thanks to Antara Rao, Katie Dorsch Smith and Olivia Pourza for all the excellent histological work included below. Thanks to my current and former lab mates Justin Elstrott, Brian Isett, Sam Harding Forrester, Toshio Miyashita, Keven Laboy, Amy LeMessurier, Philipp Schnepel, Ray Shao, Melanie Gainey, Chris Rodgers, Joe Goldbeck, Dave House, and Renna Wolfe, for their input, advice and discussions. It was truly a joy to work in the Feldman lab these last five years. Thanks to my wonderful friends for accommodating my horribly busy schedule, and sticking with me despite it. Thanks most of all to my family, without whom I would be nothing. Their faith in me has always been a self-fulfilling prophecy. I'm so incredibly proud to be my parent's daughter, and so in awe of my sisters, and humbled by their goodness. My father was the first to instill in me a great reverence for the natural world, and through his incredible dedication to saving the lives of children, he taught me that life loves nothing more than life. It is this love that motivates my science.

Chapter I, in full, is original work submitted as:
Kelly B. Clancy, Antara R. Rao, Daniel E. Feldman. Structure of the sparse code in layer 2 of mouse somatosensory cortex. The dissertation author was the primary author of this paper. It is included with permission from all authors.

Chapter II, in full, is a reprint of material as it appears in:
Kelly B. Clancy, Aaron C. Koralek, Rui M. Costa, Daniel E. Feldman, Jose M. Carmena. Volitional modulation of optically recorded calcium signals during neuroprosthetic learning, Nature Neuroscience (2014). The dissertation author was one of two primary authors of this paper. It is included with permission from all authors.

INTRODUCTION

With the evolution and expansion of the neocortex came a great leap in animal intelligence. The neocortex, a thin sheet of neurons comprising the exterior of the mammalian brain, integrates sensory and internal information in order to drive decisions and behavior. Information from peripheral sensory receptors is sent to distinct, spatially organized cortical areas for processing. The cortex is further divided into six layers, comprised of genetically specific excitatory and inhibitory cell types. This six-layered structure and basic cell types and connectivity within- and across-layers are ubiquitous among almost every cortical area, suggesting that different areas utilize canonical circuitry. In general, layer (L) 4 appears to be the major input layer, receiving information from the sensory periphery via the thalamus. L2/3, comprising most of the superficial swath of cortex, is a major output layer and remains plastic throughout adulthood. Representations of sensory features in L2/3 can grow or shrink depending on sensory input, a process known as map plasticity (Feldman, 2005).

Rodents, a nocturnal creature, are thought to rely heavily on somatosensory information, particularly from their whiskers. Using their whiskers, rodents can estimate distance in a gap-crossing task, distinguish textures and macroscopic shapes, and follow navigational cues (Morita et al., 2011; Jenkinson et al., 2000; Knutsen et al., 2006). Information from each of the ~30 contralateral whiskers on the face are thought to be processed in discrete cortical patches, known as barrel columns. This feature makes the rodent vibrissal somatosensory cortex (vS1) a favorite system for studying cortical coding. It's also ideal for plasticity studies, thanks both to this orderly mapping as well as the ease of manipulating whisker input. Cortical columns, most prevalent in higher mammals, represent orderly subdivisions of a sensory area wherein similarly tuned neurons are spatially clustered. They were once thought of as functional units of computation, however, as barrel columns are the only columns evident in mouse and rat cortex, it's unclear whether this columnar structure has any real functional role in cortical processing (Mountcastle, 2007).

Understanding how somatosensory information is processed by cortex is essential for relating sensory input to behavior. A number of insights into cortical coding have been made possible by recent technological advances in neural recordings, particularly calcium imaging *in vivo* using two-photon microscopy (Denk et al., 1990). In calcium imaging, a calcium-sensitive fluorescent indicator is introduced to a population of neurons, either by bulk-loading with a cell-membrane permeant dye (Stosiek et al., 2003), or by inducing the expression of a fluorescent protein (Tian et al., 2009). A spike in the cell creates an influx of calcium marked by a dramatic increase in the brightness of the indicator, followed by an exponential decay. This method, coupled with two-photon microscopy, enables researchers to record relatively deep in intact brains, allowing the visualization of activity in an entire local network. Additionally, different cell populations can be tagged genetically or with neural tracers in order to record activity in a high-throughput manner from a specific population of cells. Calcium imaging, however, is limited by scan rates, slow calcium dynamics, low signal to noise during single spike events, and bleaching or cytotoxicity of the calcium indicator (Looger & Griesbeck, 2012). These caveats primarily limit our ability to detect single spikes and recover

spike trains from high firing rate neurons.

Recent calcium imaging studies in rodents have revealed an unexpected heterogeneity of tuning in L2/3 of multiple sensory areas—primary visual cortex, auditory cortex and (most surprisingly, given its columnar nature) somatosensory cortex all exhibit salt and pepper tuning in superficial layers. Perhaps rodent cortex is just too small to support more orderly, cortical column-like spatial organization, despite the fact that 'minicolumns', thought to be the fundamental building blocks of cortical columns, are present in rodents. Mountcastle was the first to invoke the minicolumn, a vertical structure formed by migration of neurons from the germinal epithelium along radial glial cells (Horton and Adams, 2005). It was thought that a column is formed by many functionally similar minicolumns bound by short-range horizontal connections. In rodents, clonally related cells do maintain similar tuning (Li et al., 2012), but there is a lack of clustering into larger, functionally similar domains. While connections appear to be made preferentially between functionally similar neurons (Harris and Mrsic-Flogel, 2013), there is a significant amount of randomness as well (Ko et al., 2011). Perhaps the column is not a canonical unit of computation, but an epiphenomenal structure for minimizing wiring in relevant connections, and thus only appears in the cortex of larger mammals with more cortical 'real estate.' It might be informative to search for columns in larger rodents (e.g., capybara, guinea pigs) and the smallest primates (e.g., pygmy marmoset) in order to see whether functional columns organically form (or fail to form) depending on available cortical space.

It would also be interesting to relate the smoothness of tuning to cortical depth, as we know there is a more crystalline organization of tuning in L4. It's been surmised that layers 2 & 3, usually lumped together, represent different processing streams, especially in mice—perhaps, again, reflecting some form of economization for the sake of space. While rats have septa between their barrel columns that appear to code for complex interactions and multi-whisker dynamics, mice lack these septa, and so perhaps such computations are primarily performed in L2, which is known to receive significant multi-whisker input from L5 (Bureau et al., 2006). This may also explain the relatively low response rates recorded in L2: previous calcium-imaging studies have mapped responses to single deflections of individual whiskers, but perhaps cells are truly coding for more complex whisker interactions. Unexpectedly, longitudinal studies have also indicated that the tuning of individual cells is not stable over days (Margolis et al., 2012), but this may only reflect noise in unreliable responses to a sub-optimal stimulus. By determining the best stimuli for driving reliable L2/3 responses and pairing this stimuli set with more sensitive calcium indicators, we should better understand this strange phenomenon.

In addition to the heterogeneity of tuning in superficial cortex, calcium imaging has revealed new insights about the responsivity of neurons. Early extracellular recordings in cortex led researchers to believe that the brain was incessantly active, and that neurons fired spikes robustly at rates of tens of hertz or more. This, along with other evidence, underpinned the view that time-averaged firing rates, rather than individual spikes, might be the relevant information-carrying signal in the brain. Yet a discrepancy became apparent: extracellular recordings in cortex and hippocampus typically yield data from about 10% of the theoretical maximum number of neurons from which they should have be able to record, suggesting there was a 'dark matter' problem in neuroscience (Shoham et al., 2006). Because

extracellular electrodes can only record from active neurons, less- or non-active cells are essentially invisible to such methods. It was suggested that tissue compression and damage from electrode insertion might render local neurons less active, but with the advent of less-invasive recording techniques, it has become apparent that much of the cortex is indeed incredibly quiet (de Kock, et al., 2007; de Kock, et al., 2009; Brecht, 2003).

Calcium imaging studies, in conjunction with less-biased recordings like cell-attached and whole cell recordings in vivo, have made it clear that a large population of neurons appear to spike rarely, or never. In S1, responses are binary: a neuron will respond to a stimulus with either 0 or 1 spikes. This underscores the importance of single spikes, rather than rate coding, in cortical computations. There are a number of computational and metabolic benefits to minimizing the spikes needed to represent a stimulus, known as 'sparse coding' (Olshausen and Field, 2004). As spikes are metabolically costly, it makes sense that neural systems might be optimized to encode information with the minimum of spikes. Sparse coding strikes a balance between a dense code, which requires few neurons but fail to reliably distinguish between subtly different stimuli, and a grandmother cell code (the logical extreme of a sparse code), which require a huge population of neurons, each narrowly tuned for an incredibly specific parameter (e.g. one's grandmother).

However, it's not simply that a small number of spikes are distributed among the population—in the traditional sparse model, cells are heterogeneously tuned for salient features, but otherwise have relatively homogenous response properties including similar maximal firing rates to optimal stimuli (Olshausen and Field, 1996). Instead, across many different brain areas and behavioral states, there appears to be a gradient of activity, wherein the majority of spikes are elicited from a minority of neurons (Buzsaki and Mizuseki, 2014). There does not appear to be distinct populations of active and silent cells, but rather a long tail of more responsive cells in a skewed distribution. By fluorescently tagging more active cells using GFP coupled to c-fos, an immediate-early gene, researchers have determined that these more active cells are preferentially interconnected (Yassin et al., 2010). In addition, the more responsive L2/3 cells receive stronger excitatory drive from L4. Thus, they not only have privileged access to the network, but they preferentially share this information with each other. Unlike tuning, a neuron's identity as high- versus low-responsive seems to be stable over days of adult experience (Margolis et al., 2013). It would be interesting to study when this network becomes established in a developing animal—whether these cells are in some way genetically determined, or whether this more-active network organically forms as initially equally-connected cells battle in a winner-take-all scenario.

This skewness appears to be a ubiquitous feature of the brain. Across many scales, the distribution of physiological and anatomical features follow a skewed distribution. Spine head size, axonal calibres, local field potentials, firing rates, synaptic strengths and the connectivity profiles of neurons all follow log-normal distributions (Buzsaki and Mizuseki, 2014). What is the advantage of this organization? It would be metabolically costly to maintain a large pool of neurons that rarely or never spiked, unless they played some important role. Perhaps the existence of a small, preferentially connected subset of neurons represent a network for making fast decisions or detections, i.e. that *something* happened, whereas the remaining population effectively code for (slower) discriminations, and contribute precision as to *what* happened. By tagging the more-active network with cFos-Cre and expressing neural silencers

like halorhosopsin, we might better understand the role of the more active network in different behaviors.

It's also been argued that the silent neurons might serve as a 'reserve pool' for plasticity (Barth & Poulet, 2012). One study which tracked their fate over the course of a plasticity manipulation suggests this might be true (Margolis et al., 2012), but more work is still needed. Another interesting avenue of future work would be to investigate whether silent cells can be 'trained' to become more high-active cells by coupling their activity to a behaviorally salient stimulus. In one study discussed below, we trained mice to control a brain machine interface, which gave us direct control over which cells learned a task. By coupling the activity of a particular cell or group of cells to reward, we found animals could learn to volitionally modulate firing patterns, and that we could induce much higher firing rates in even non-spiking cells. Further work using this technique would be invaluable to elucidate how, exactly, such volitionally-induced changes in excitability are elicited.

It might be that the unexpectedly low responsiveness observed in rodent cortex reflects the anesthetic state, but even awake, behaving animals display low firing rates (O'Connor et al., 2010b). Response rates are, however, also locomotion dependent (Niell et al., 2010), and a number of studies have reported that some fraction of cells in a given cortical area code for a different sensory modality (Yaka et al., 1999). Additionally, we found that animals could be trained to exert volitional control over the firing of neurons, even in S1. Finally, tuning and responsiveness can be influenced by experience (fear conditioning, environmental enrichment, cross-modal plasticity). It's becoming clear that neurons in primary sensory cortices are not purely driven by information impinging from distant peripheral sensors. Neural activity is dictated by a number of many non-sensory related signals, reflecting fear memories, internal and external states, and even volitional control: there is much more state-dependence on cortical computations in primary sensory areas than was expected.

Novel tools, including calcium imaging, have yielded a great number of insights into the computations performed by the cortex. Fractured tuning, low response rates, and strong volitional modification are all unexpected features of the neural code in rodent S1. While it no longer seems that neural circuitry is necessarily interchangeable between different sensory cortical areas, there is still something fundamental about the kinds of computations each area performs: likely it is function, and not form, that is preserved.

I. STRUCTURE OF THE SPARSE SPIKE CODE IN LAYER 2 OF MOUSE SOMATOSENSORY CORTEX

INTRODUCTION

Individual whisker stimuli evoke few action potentials in rodent somatosensory (S1) cortex, an example of sparse sensory coding. Layer (L) 2/3 is particularly sparse, with single-neuron whisker responses being mostly binary (0 or 1 spikes) and strikingly unreliable (mean response probability [Pr] ~0.1 per deflection), yielding low firing rates during whisker behavioral tasks. Moreover, Pr is highly skewed across L2/3 neurons, with most neurons having very low Pr (<0.1) to deflection of the columnar whisker, and only ~10% of neurons having higher Pr (~0.2-0.6) and generating most whisker-evoked spikes. How this code is organized and implemented in L2/3 circuits remains unclear.

Multiple factors can generate sparse spiking, including heterogeneous sensory tuning, inherently low responsiveness among similarly tuned neurons, and subcircuits with varied responsiveness. In classical sparse population coding, sparse firing is due to heterogeneous sensory tuning among otherwise equivalent pyramidal cells, each of which responds strongly and reliably to its optimal stimulus. This causes sensory stimuli to activate a small, stable subset of neurons. Alternatively, sparse spiking may derive from inherently low trial-to-trial Pr among similarly tuned neurons, resulting in a small, shifting ensemble of spiking neurons across trials. This may be a primary factor in S1, where Pr is low, whisker somatotopic tuning is largely homogeneous within each cortical column, and tuning for other whisker parameters is relatively broad. The skewed Pr distribution in S1 may reflect either sensory tuning for the applied stimuli, or a spectrum of inherent responsiveness across pyramidal cell subclasses, interneuron classes or processing streams.

We investigated the relative importance of these factors in generating sparse spiking in mouse S1, focusing on L2, where spiking is sparsest. Prior studies of L2 population coding measured neural responses only to the column-associated whisker or one neighbor. However, substantial paralemniscal and cross-columnar input to L2 could confer heterogeneous whisker tuning, sparsening population activity. We used 2-photon calcium imaging with Oregon Green BAPTA-1 AM (OGB-1 AM) to characterize whisker responses in L2 of anesthetized mice. Stimulating 9-15 whiskers, we observed highly heterogeneous whisker tuning among co-columnar neurons. By measuring Pr to each neuron's individually determined best whisker and spontaneous activity, we found a prominent spectrum of inherent responsiveness across neurons. Whisker tuning and Pr differed between S2- and M1-projecting neurons. Whisker tuning and low Pr both contributed to sparse coding, with different levels of sparseness across different S1 output streams.

RESULTS

Population Ca^{2+} imaging in S1

We imaged whisker-evoked activity in dense populations of L2 neurons in mouse S1 by bolus injecting the calcium indicator OGB-1AM into a functional whisker-related column (C1-3, D1-3, or E1-2) identified by intrinsic signal imaging. Activity was measured using 2-photon imaging in 20-50 neurons in a ~160 x 160 μm field (about the size of an anatomical whisker column), at 120-180 mm depth corresponding to L2. Whisker stimuli were single, independent deflections of 9 or 15 neighboring whiskers in a square array (Figure I-1A-E). Discrete calcium events corresponding to spikes or spike bursts were identified from DF/F traces by non-

negative deconvolution. The sensitivity of spike detection was calibrated by simultaneous cell-attached recording (n = 15 cells) (Figure I-1F). Deconvolution detected 55% of single spikes (within 140 ms, a single imaging frame) and 90% of spike doublets, with a false positive rate of 0.05 Hz.

We measured OGB-derived Ca^{2+} events for all neurons in each imaging field during whisker stimulation and interleaved epochs of spontaneous activity. For each neuron, we quantified whisker-evoked response probability (Pr) and identified the principal whisker (PW) as the whisker that evoked the highest Pr. The most common PW across neurons in an imaging field was designated the field best whisker (FBW). Post-hoc reconstruction of imaging field location relative to the anatomical barrels in layer 4 showed that FBW identity matched anatomical barrel identity in the imaging field center in 6/6 cases (Figure I-2).

Highly divergent whisker tuning in a single cortical column

In classical extracellular recording studies in rats, >80% of barrel column neurons are tuned to the anatomically matched whisker. However, this likely omits low-responsive cells, which are the majority of cells in L2. In addition, it is unclear if the same tuning would occur in mouse L2, which receives extensive paralemniscal and cross-columnar input. We measured whisker tuning to 9 or 15 whiskers (50-150 repetitions each), unlike prior studies that used only 1-2 whiskers. L2 neurons showed remarkable local heterogeneity in somatotopic whisker tuning, measured as mean Pr to each sampled whisker. Figure I-3A shows an example imaging field in which D2 was the FBW, but that contained numerous strongly responsive neurons tuned to E1, E2, D1, D2, D3, C1, and C2 whiskers. Other example fields are shown in Figure I-4. Divergent tuning was also observed with the genetically encoded calcium indicator GCaMP6f (example field, Figure I-3D-F). Significance of tuning was verified by calculating 95% confidence intervals for Pr for each whisker, assuming Poisson statistics (Figure I-4). While many cells were driven by the PW significantly more than any other whisker, other cells responded equally to several neighboring whiskers (Figure I-4). Tuning heterogeneity was also evident in average DF/F traces without deconvolution (Figure II3C and F, Figure I-4B).

We quantified the diversity of whisker tuning across all imaging fields (1659 neurons, assayed with either 9 whiskers [46 fields, 24 mice], or 15 whiskers [5 fields, 3 mice]). 25% of neurons (422) were tuned to the FBW, 11% to same-row, adjacent-arc whiskers (181), 12% to same-arc, adjacent-row whiskers (195), and 11% to adjacent-arc, adjacent-row ("diagonal") whiskers (185). 19% were tuned to more distant whiskers, and 22% of neurons were unresponsive to all presented stimuli (defined as $Pr < 0.05$) (Figure I-5A-B).

Whisker receptive fields of individual neurons were narrow, on average, with immediate surround whiskers evoking 38 ± 3% Pr compared to the PW (Figure I-5C). Whisker tuning of entire imaging fields (compiled across all cells) was much broader, with whiskers immediately adjacent to the FBW evoking 65 ± 5% Pr compared to the FBW (Figure I-5D). To compare tuning width statistically, we calculated whisker selectivity index (WSI), defined as Pr to the best whisker (for one neuron or the entire field) divided by the average Pr to immediately neighboring whiskers. WSI was significantly greater for single neurons than for fields ($p=5.9e-16$, KS test) (Figure I-5E). Thus, local fields are composed of individual neurons with narrow, somatotopically heterogeneous whisker tuning.

To test whether co-tuned neurons are functionally related in other ways, we measured

the correlation between calcium event trains for pairs of neurons during spontaneous activity periods. Pair-wise correlations fell off with distance between neurons; however, neurons tuned to the same PW showed higher correlations than neurons tuned to different PWs (Figure I-6). This finding is similar to results in visual and motor cortex, and suggests that co-tuned neurons are organized into distinct subnetworks.

Size and columnar organization of the ensemble activated by each whisker

From each cell's Pr to the FBW and nearby whiskers, we calculated the average size and columnar organization of the L2 neuron ensemble activated by each whisker (Figure I-7). In each local field, 25%, 6%, 5.5% and 2.8% of cells were tuned to the FBW, or to one immediately adjacent row, arc, or diagonal whisker, respectively. The set of neurons co-tuned to one whisker (here called the tuning ensemble) is therefore distributed across columns. Because most neurons exhibited weak non-zero responses to multiple surround whiskers, the minimally responsive ensemble to each whisker (defined as all neurons with Pr > 0.05) was much larger, with 58%, 44%, 41%, and 41% of neurons being at least minimally responsive to the FBW or immediately adjacent row, arc, or diagonal whisker. However, Pr was very low for most neurons, even for the PW (analyzed in detail below). Because of this, the single-trial spiking ensemble to each whisker (defined as the number of neurons that spike, on average, to each whisker deflection) was much smaller: only 6.8%, 5.1%, 4.9%, and 4.8% for these whiskers (Figure I-7A). Because we detected only 55% of single spikes (Figure I-1F), the true size of the spiking ensemble may be 9-12% of L2 neurons.

These results are replotted in Figure I-7B to schematize the tuning, minimally responsive, and spiking ensembles in L2 across multiple S1 columns in response to a single rostral deflection of the center-column whisker under our anesthesia conditions. All three ensembles are spread across multiple cortical columns, with the single-trial spiking ensemble being much smaller than the minimally responsive ensemble, and only partly overlapping with the tuning ensemble (because spikes are evoked in neurons with peak tuning to nearby whiskers). This representation ignores variations in Pr with distance from column center, and mapping of direction tuning.

Skewed distribution of more-responsive and less-responsive neurons

Pr to the FBW (Pr_{FBW}) was low, and skewed across the L2 neuron population: mean Pr_{FBW} was 0.09 (Fig. I-8A, solid curve), and 35% of neurons were unresponsive to FBW, defined as $Pr_{FBW} < 0.05$. This confirms prior studies that showed weak whisker responses in L2/3 with a small tail of more responsive neurons. Responsiveness of each neuron to its individually determined PW (Pr_{PW}) were somewhat stronger: mean Pr_{PW} was 0.12, and only 16% of neurons were unresponsive (Figure I-8A, dashed curve). Thus, Pr was 33% greater when assayed with the individually determined best whisker, but was still quite low overall. The Pr_{PW} distribution remained skewed after subtracting spontaneous firing rate (Fig. I-8A, bars). All remaining analyses report Pr_{PW} with spontaneous firing rate subtracted.

Impact of column-specific tuning on P_r

The factors that underlie the skewed distribution of P_r in S1 are unclear. We first tested whether neurons tuned to different PWs within the same imaging field had systematic

differences in P_r. Neurons with high Pr_{PW} were only slightly more likely to be tuned to the FBW than neurons with low Pr_{PW} (Figure I-8B). High Pr_{PW} neurons were more narrowly tuned as measured by WSI, and narrowly tuned neurons thus had slightly higher Pr_{PW} (Figure I-8C-D). Only whisker-responsive neurons were included in this analysis. Thus, tuning to the column-specific whisker vs. other whiskers only modestly impacted Pr_{PW}.

Spontaneous firing rate strongly predicts P_r

S1 may contain subnetworks of inherently more active neurons, independent of stimulus choice. To test this idea, we compared Pr_{PW} with spontaneous activity rates, which are not determined by experimental stimulus choice. Spontaneous rates were stable across hours of imaging (2677 cells in 51 animals, t-test early versus late mean spontaneous rate, p=0.83), and did not appear to be affected by epochs of stimulation. We observed a broad range of spontaneous activity rates (Figure I-9A), and found that spontaneous rate was strongly correlated with Pr_{PW} (Figure I-9B, R^2=0.32, p < 1e-16). Cells with high Pr_{PW} were also more responsive to non-PW whiskers (Figure I-9C, R^2=0.69, p<1e-14), consistent with a generally more responsive subset of neurons. Pr_{PW} was not correlated to SNR, ruling out an artifact of OGB loading or imaging noise (Figure I-9D, R^2=0.02, p=1.5e-13). On the population level, cells with high spontaneous rate dominated the population of high Pr_{PW} cells (Figure I-9E), as observed in A1. The correlation between spontaneous rate and Pr_{PW} was also significant for raw DF/F and for unthresholded deconvolved data (Figure I-10). Thus, a spectrum of inherent responsiveness exists in L2, independent of stimulus choice.

High P_r cells include both pyramidal cells and interneurons

High Pr_{PW} cells may be interneurons, which have substantially higher spontaneous firing rates than pyramidal cells in L2/3. High Pr neurons in our dataset are unlikely to be fast-spiking (FS) interneurons, because the high firing rate of these cells obscures discrete spike-evoked calcium events that would be detectable by the deconvolution method. To test what fraction of high Pr_{PW} neurons are interneurons, we imaged whisker-evoked responses in GAD67-GFP heterozygous mice, which label all interneurons with GFP (Figure I-11). Only 3 whiskers were stimulated in these experiments. Interneurons showed significantly higher spontaneous event rates than GFP-negative neurons (putative pyramidal cells) (p=0.002, KS test), and showed a non-significant trend for higher Pr_{PW} (p=0.08). However, the high Pr_{PW} population included both putative pyramidal cells and interneurons (Figure I-11E-G).

Tuning and sparseness differ between M1- and S2-projecting neurons

Sparse coding may vary across different functional streams within S1, including pyramidal cell subclasses that project to different targets, consistent with functional specialization of different output neurons. Output targets of L2 of S1 include primary motor cortex (M1) and secondary somatosensory cortex (S2), with only modest overlap (1-10%) between these populations. To compare whisker tuning and sparse coding between these populations, we labeled M1-projecting (M1p) neurons or S2-projecting (S2p) neurons in separate experiments by injecting the retrograde tracer CTB-Alexa594 into either M1 or S2. After allowing time for CTB transport, we imaged in S1 and recorded activity from M1p or S2p neurons and unlabeled neurons (the latter represent both neurons that do not project to M1/S2 and an unknown

fraction of unlabeled M1p/S2p neurons) (Figure I-12). M1p neurons (Figure I-12A) had similar Pr_{PW} to unlabeled cells (Figure I-12B, p=0.3, KS test) but were more broadly tuned (Figure I-12C, p=0.04), as reported previously. M1p neurons were equally likely to be tuned to the FBW as unlabeled neurons (p=0.3, binomial test, Figure I-12D).

In contrast, S2p neurons (Figure I-12E) had significantly higher Pr_{PW} than unlabeled neurons (Figure I-12F, p=0.009, KS test) and were more narrowly tuned (Figure I-12G, p=0.04). S2p neurons were more likely to be tuned to the FBW than unlabeled or M1p neurons (Figure I-12D, p=0.02, binomial test). These results differ from a prior study in which S2p neurons did not differ in Pr or relative response to 2 whiskers (FBW and one neighbor). When we restricted our analysis to these 2 whiskers, these effects were not significant. Thus, S2p neurons differed only when a broader range of tuning was considered. M1p and S2p neurons did not differ in spontaneous firing rate. Overall, the projection target of L2 cells had a measurable effect on a neuron's place in the Pr_{PW} distribution (Figure I-12H).

Inter-areal projections may be bottlenecks for the flow of information in cortical sensory processing, comparable to narrow cables in data networks. Theoretical analysis suggests that projections with fewer axons may require greater data compression (denser spike coding) to preserve information compared to projections with more axons. To test this idea, we compared axon number and coding sparseness in the S1→M1 and S1→S2 projections. To determine the relative number of axons on each projection, we made a single focal injection of AAV2.9-CAG-Flex-tdTomato-WPRE-bGH virus into S1 of Drd3-Cre mice, which express Cre largely in L2/3 pyramidal neurons. tdTomato was expressed strongly in L2/3 pyramidal neurons at the S1 injection site (Figure I-13A), with 10% off-target expression in L5 pyramidal cells. In each mouse (n = 3), we counted the number of tdTomato-labeled axons entering S2 and M1 (235 ± 22 and 463 ± 29 axons, respectively). The within-mouse S2p:M1p axon ratio (originating from the same S1 injection site) was 0.50 ± 0.06 (Figure I-13D). To compare coding sparseness between these projections, we examined the coding of FBW deflection in each column by S2p and M1p neurons. Population sparseness was calculated using a well-established metric, S_p, which is related to the proportion of highly responsive cells within the population. S_p ranges from near 0% (a dense code) to 100% (a sparse code). Across all L2 neurons (i.e. the same dataset as Figs. II3-9), S_p for FBW deflection was 0.45. M1p neurons and unlabeled neurons in M1p- and S2p-labeled mice were similarly sparse (0.41-0.42). S2p neurons showed significantly less sparse coding (S_p = 0.29; p=0.02 vs. unlabeled neurons in the same experiments, KS test, Figure S5E). This likely reflects the higher Pr_{PW} and greater proportion of FBW-tuned neurons among S2p neurons (Figure I-12). Thus, the projection with fewer axons (S2p) exhibited denser spike coding, suggesting that differences in Pr between M1p and S2p neurons may partially reflect distinct data compression requirements related to axon number on these projections.

DISCUSSION

Sparse sensory coding is common in rodent sensory cortex, but the structure of the sparse code and its basis in sensory tuning, low inherent responsiveness, and circuit-level specializations are not well understood. We combined 2-photon OGB-1 calcium imaging with deflection of many whiskers to study sparse coding in whisker column-sized imaging fields in S1. Due to the relatively slow dynamics of calcium dyes, calcium imaging is not ideal for reporting rapid firing

rates (e.g. fast-spiking interneurons), but is well suited to report spiking of L2/3 pyramidal cells. The organization of the L2 population code was not clear from prior cell-attached recordings (due to small sample size) or extracellular single-unit recordings (due to bias against low-spiking neurons). Prior population calcium imaging studies identified important features of L2 coding but did not address tuning to more than one non-columnar whisker.

We found that whisker somatotopic tuning in L2 was highly diverse locally, with salt-and-pepper organization at the microscopic level but somatotopically correct mean tuning at the population (columnar) level, consistent with a prior study that measured responses to 2 whiskers. Response probability to each neuron's individually determined best whisker was low (mean: 0.12) and skewed with a small tail of more-responsive neurons, also consistent with prior studies. Pr_{PW} was predicted strongly by spontaneous firing rate but only weakly by tuning properties, indicating that a substantial component of responsiveness is independent of stimulus choice. Higher-responsive neurons included both interneurons and pyramidal cells. Whisker tuning and Pr varied between M1p and S2p neurons, with S2p neurons encoding the column-specific whisker using a denser spike code than other cells. Thus, sparse coding in L2 reflects combination of heterogeneous sensory tuning, low inherent responsiveness organized in a skewed spectrum across neurons, and functional specialization across S1 output streams.

Heterogeneous whisker tuning in single S1 columns

In rodent visual and auditory cortex, maps of sensory features are smooth on the macroscopic (column) level, but at the microscopic level neurons tuned for different features are intermixed in a salt-and-pepper organization. Similar salt-and-pepper somatotopy was known in S1 for relative tuning to two whiskers. Using 9-15 whiskers, we found marked heterogeneity of whisker tuning, with only 25% of L2 neurons tuned to the column best whisker, 34% tuned to adjacent and diagonal whiskers, and 19% tuned to distant, non-adjacent whiskers (Fig. 3). Thus, the set of neurons co-tuned for one whisker was scattered sparsely across multiple columns (Fig. 4).

Extracellular single unit recordings in rats show that > 80% of L2/3 neurons are tuned to the column-associated whisker. Heterogeneous whisker tuning in mouse L2 may derive from prominent paralemniscal L5a input and cross columnar input, similar to septa-related columns in rats. Despite local tuning diversity, average tuning across all local neurons matched expected somatotopy for the whisker column, confirming the prior results with 2 whiskers. Thus somatotopic tuning precision in L4 appears to decrease in the projection to L2, consistent with integration with paralemniscal and cross-columnar inputs and similar to auditory cortex. Direction tuning is another source of tuning heterogeneity in L2/3, but was not studied here.

The skewed Pr distribution reflects a spectrum of inherent responsiveness

We found that low average Pr was the major factor generating the sparse, shifting set of neurons in response to a single whisker deflection. Prior studies demonstrated a skewed distribution of Pr across L2/3 neurons, with most neurons having low Pr, and a small population of high-Pr neurons generating most whisker-evoked spikes. However, whether Pr variation reflected tuning to the applied whisker stimulus, or instead reflected a spectrum of inherent responsiveness across neuron classes, was unclear. We found that Pr to each neuron's individually determined best whisker (Pr_{PW}) was also skewed. Pr_{PW} correlated weakly with

tuning properties (Fig. 5) but strongly with spontaneous firing rate (Fig. 6), as in auditory cortex. Thus, a substantial component of responsiveness is independent of stimulus choice. More active cells included both interneurons, as expected, and also many pyramidal cells (Fig. 7). These results are consistent with the existence of a more active subclass of pyramidal cells that receive greater excitation from the local network.

The point representation of a whisker in L2

Based on our data, we define three distinct whisker-related neuronal ensembles: the tuning ensemble (the set of neurons with peak tuning for a whisker), the single-trial spiking ensemble (the average set of neurons that spike to one whisker deflection), and the minimally responsive ensemble (the complete set of neurons with non-zero Pr; that is, the full set of neurons that may spike over a large number of deflections). All three ensembles are distributed sparsely across several columns, due to heterogeneous whisker tuning (Fig. 4). Low Pr causes the single-trial spiking ensemble to be a small, shifting subset of the minimally responsive ensemble. Because neurons are not tuned purely to single whiskers, the single-trial spiking ensemble includes many neurons outside the tuning ensemble. These findings predict that decoding of whisker identity from L2 population activity will be more efficient if population activity is sampled from within tuning ensembles, rather than within anatomical columnar modules. This is distinct from L4 of S1, where homogeneous whisker tuning minimizes information loss when pooling within columns.

Specializations of S2 and M1 output pathways

Cortical pyramidal neurons projecting to distinct long-range target areas can exhibit specialized sensory tuning and firing patterns. In S1, M1p and S2p pyramidal cells differ in sensory tuning, intrinsic biophysical properties, recruitment during different behavioral tasks, and dynamics of whisking- and contact-related spikes. By receptive field mapping across many whiskers, we found that S2p neurons were more narrowly tuned than other neurons, were more likely to be tuned to the column-related whisker, and had higher Pr_{PW}. In contrast, M1p neurons were more broadly tuned to multiple whiskers (Fig. 8), as in a prior study. M1p and S2p neuronal identity modestly predicted a neuron's position on the Pr_{PW} distribution (Fig. 8).

Theoretical work suggests that area-to-area projections containing few axons may constitute information bottlenecks that require data compression for effective information transmission. Such compression may take the form of a denser spike code. We found that the S2p projection contains roughly half as many axons as the M1p projection, and that correspondingly, S2p neurons code for FBW deflection more densely than M1p neurons—that is, FBW deflection drives a stronger spiking signal among S2p neurons than M1p neurons (Fig. S4). This is consistent with the recent finding that S2p neurons exhibit stronger, more sustained spiking during active touch than M1p neurons, and are more synaptically excitable. Thus, S2p and M1p subpopulations send different whisker information, coded with different degrees of sparseness, to their target areas.

SUMMARY

Sparse coding in L2 of S1 reflects a combination of locally heterogeneous whisker tuning, low inherent response probability, a skewed spectrum of responsiveness across neurons, and

specializations between S2 and M1 output streams. These factors cause single whisker deflections to elicit sparse spikes in small, shifting ensembles of L2 neurons spanning many cortical columns. This sparse, somatotopically divergent code is a substantial transformation from L4, where Pr is higher and the large majority of neurons are tuned for the column-appropriate whisker. While somewhat stronger spiking is expected in awake animals, the functional contribution of the large number of low-responsive neurons remains unclear. Some may be tuned to multiwhisker or other complex input, while others may be a reserve pool to be recruited during plasticity, or in specific behavioral tasks by association with reward.

METHODS

All procedures followed ACUC and NIH guidelines. Male mice (P30-45) were used (n = 38 C57BL/6J, 4 GAD67-GFP, 3 Drd3-Cre). GAD67-GFP mice were provided by Yuchio Yanagawa, bred with C57BL/6J mice, and heterozygotes offspring were used for experiments.

Surgical preparation, intrinsic imaging, and OGB bulk loading

Mice were anesthetized with urethane (1.2 g/kg) and chlorprothixene (0.08 mg), and anesthesia was maintained with supplemental urethane as needed. A stainless steel head holder and imaging well was affixed over S1 (1 mm posterior, 3 mm lateral to Bregma). The location of D1-3 whisker columns was mapped through the intact skull using intrinsic signal optical imaging, as in. A 1 mm craniotomy was made.

For OGB-1 bulk loading, 50 µg OGB-1 AM (Life Technologies) was dissolved in 5 µL of 20% Pluronic F127 in DMSO (Teflabs), and then diluted 10-20 fold in buffer (in mM, 150 NaCl, 2.5 KCl, 10 HEPES). This solution was pressure ejected (3 PSI, 1-5 min) from a 3 µm tip pipette at 250 µm below the pia, centered in the intrinsic signal response area of one whisker. Surface blood vessels were used for alignment. The pipette was removed and dye was allowed to load for ~1 hour before imaging. Typically, cells within ~250 µm radius were loaded. A glass coverslip was mounted via a locking ring to minimize brain pulsation.

GCaMP6 injection

For GCaMP6 experiments, P22-25 mice were anesthetized using isoflurane, placed in a stereotax with body temperature maintained at 37°C, and a small craniotomy was opened over S1. 150 nL of recombinant viral vector (AAV2.9 Syn.GCamp6f.WPRE.SV40; University of Pennsylvania Vector Core) was delivered 300 mm below the pia using a Nanoliter injector. The scalp was sutured and the animal recovered. 2-3 weeks later, calcium imaging was performed under urethane/chlorprothixene anesthesia, as described above. Data from gCaMP6 mice were not included in the OGB population data, and were solely used to confirm heterogeneous whisker responses in L2/3.

2 photon calcium imaging and whisker stimulation

Imaging was performed with a Moveable Objective Microscope (Sutter, Novato CA) and Chameleon Ultra Ti:Sapphire mode-locked laser (Coherent, Santa Clara CA). OGB-1 and Alexa 594 were excited at 800 nm, and GCaMP6f and GFP were excited at 920 nm. Red and green emission were separated Chroma HQ 525/50 and 575/50 filters and detected with Hamamatsu photomultiplier tubes (H10770PA-40). Using a Nikon objective (16x, 0.8 NA), movies (100 sec,

7.23 Hz frame rate, 128 x 512 pixel frame size) were collected using ScanImage. Each field was imaged for 80-120 minutes, interleaving spontaneous and stimulus-evoked epochs. 1-6 fields were imaged per mouse.

Whiskers were deflected using a 3 x 3 or 4 x 4 array of calibrated piezoelectric actuators, each attached to a single whisker. Single rostrocaudal deflections were used (4º amplitude, 4-ms ramp and return, 100-ms hold, delivered 3 mm from skin). Stimuli were delivered at 3-5 s isi, interleaved across whiskers.

In GAD67 mice, GFP-labeled neurons were identified after separating GFP and OGB fluorescence by subtracting an image with 920 nm excitation (peak GFP excitation) – an image with 800 nm excitation (peak OGB1 excitation). This subtraction was only used to identify GFP+ neurons, and was not carried through the DF/F calculation.

Imaging data analysis

Any movies with large transients induced by breathing or heartbeat artifacts were discarded from analysis. Movies were corrected for slow drift in the x-y plane using TurboReg in ImageJ. Although TurboReg requires that any motion in the preparation is slower than the frame rate, because the animals were anesthetized, our main source of motion was slow drift in the tissue. We tested the stability of our imaging as follows. In a randomly selected subset of data, 5 fields from 5 animals, we selected 2-3 bright astrocytes for reference. We tracked the centroid of these astrocytes frame by frame, and used this to estimate instantaneous transients from differences in this value. The maximum distance between the centroid from one frame to the next never exceeded 1.2 pixels, and therefore was highly unlikely to affect the motion correct algorithm. Over the course of an entire imaging session, the slow drift averaged 7.3 pixels per hour, or 2.0e-4 pixels per frame. Any frames with severe z-motion were excluded from analysis.

Regions of interest (ROIs) were manually selected in ImageJ to include all neuronal somata that appeared in all movies. All other analysis was performed in Matlab. Traces of relative fluorescence change, DF/F, were calculated for each ROI. DF/F= (Fi-F0)/F0, where Fi is the instantaneous fluorescence value of a cell in one frame, and F0 its average fluorescence value over the preceding 4 seconds. Positive deconvolution was used to estimate the instantaneous probability of Ca^{2+} events, which was thresholded to extract an event train for each cell. The event threshold was determined based on cell-attached recordings (n=15 neurons, Fig. 1F). Spontaneous event rates were determined from deconvolved event trains. Because the whisker stimulation was 110 ms, and spikes can occur up to 50ms after whisker deflection, we considered any event with 2 frames after the whisker stimulus onset to be a stimulus-evoked response. Reported Pr values are whisker-evoked Pr – spontaneous event rate, unless specified otherwise.

Astrocytes were excluded from the analysis based on their extreme brightness and, as they preferentially take up OGB1. In a subset of experiments, we included 1um of sulforhodamine in our OGB solution to selectively label astrocytes. We found that astrocytes were clearly identifiable by their brightness, morphology and calcium dynamics.

Signal-to-noise ratio (SNR; Fig. 6D) was calculated by dividing the average ΔF/F over all detected events by the standard deviation of baseline. To assess the significance of whisker tuning, we calculated 95% confidence interval (CI) by simulating Poisson-distributed responses to each whisker, based on mean P_r and actual number of stimulus presentations. Whiskers

whose 95% CI overlapped with the PW were considered equally responsive (red x's in Figure I-3 and I-4). For population analysis, neurons with $Pr_{PW} \leq 0.05$ were considered unresponsive. Only responsive neurons were included in analyses of tuning width or PW identity.

Population sparseness, S_p, was calculated after as $S_p = (1-\{[\sum^{N}_{j=1} Pr_j/N]^2 / \sum^{N}_{j=1} [Pr_j^2/N]\})/ (1-1/N)$, where N is the number of neurons and Pr_j is Pr for neuron j.

Cell attached calibration of spike detection

OGB-1 loaded neurons were patched under 2-photon guidance, using a recording pipette (3 µm tip, 3-5 MΩ) filled with fluorescent HEPES-buffered Ringers (in mM: 126 NaCl, 20 HEPES, 2.5 KCl, 2 CaCl2, 1.3 MgSO4, 14 D (+)Glucose, 50 Alexa-594; pH 7.3, 290 mOsm). A loose seal configuration was obtained, and spike-associated currents were measured in voltage clamp mode with holding potential adjusted to maintain a holding current of 0 pA. Spikes from the loose seal recording were collected simultaneous to OGB imaging with Ephus software. Spike times were binned to match imaging frames and compared to the calcium event train determined from deconvolution of the OGB signal.

Histological localization of imaging fields relative to anatomical barrels

In a subset of experiments, imaging fields were localized relative to anatomical boundaries of whisker-related barrel columns. To do this, low-power images of the calcium imaging field and surrounding surface blood vessels were obtained on the 2-photon microscope. The brain was then removed, fixed with 4% paraformaldehyde, and flattened. 150-µm thick tangential sections were cut, preserving the surface blood vessels, and stained for cytochrome oxidase activity to reveal L4 barrels. Barrel boundaries were projected onto the surface vessel map, which was then aligned to the low-power images of the calcium imaging field.

Retrograde tracer injection

P22-25 mice were anesthetized with isoflurane, placed in a stereotax, and body temperature was maintained at 37°C. S2 was localized via intrinsic signal imaging through the intact skull. S2 appeared as a strong intrinsic signal focus lateral to S1, typically at ~1.2 mm caudal, 4.2 lateral to Bregma. M1 was targeted stereotaxically at 1.0 mm rostral, 0.7 mm lateral to Bregma. A small craniotomy (~0.5 mm) was opened over either M1 or S2. 200 nL of CTB-Alexa594 (10 µg/µL in phosphate-buffered saline; Life Technologies, C-22842) was injected via a glass pipette (tip diameter 40-60 µm) 500 mm below the pia. Injection was performed using a Nanoliter 2000 (WPI) at 20 nL/min for 10 min, with a 10 min pause before pipette withdrawal to prevent backflow. The scalp was sutured and the animal recovered. Calcium imaging was performed in S1 5-12 d later to allow tracer transport.

Relative number of S1→M1 and S1→S2 axons

L2/3 pyramidal cells in S1 were labeled with cytosolic tdTomato by injecting 0.1 mL of AAV2.9-CAG-flex-tdTomato-WPRE-bGH viral vector (UPenn Vector Core) into S1 of Drd3-Cre mice (Allen Brain Institute, KI196 strain) at P30. After 3 weeks, mice were perfused and the brain cut coronally (50 mm sections). In S1, 91% of tdTomato-labeled neurons were L2/3 pyramidal cells and 9% were L5 pyramidal cells. Labeled axons projected to M1, S2, perirhinal cortex and contralateral S1, which are known cortical targets of S1. We counted S1→M1 and S1→S2

axons as they crossed planes marking the S1-M1 and S1-S2 boundary (dashed lines in Figure I-13), using a 63x objective and epifluorescence microscope. The S1-M1 plane was 1.5 mm from midline, perpendicular to the cortical surface, and spanned from 1 mm rostral to 2 mm caudal of Bregma. The S1-S2 plane was 4 mm from midline, perpendicular to the cortical surface, and spanned from 1 to 2 mm caudal of Bregma. Axons traveling in the white matter were excluded, as visual analysis suggested that they passed M1 and S2 for more distant targets. Axon numbers were summed across all sections, and the number of M1p and S2p axons (originating from the same S1 injection) were compared within individual mice.

FIGURES

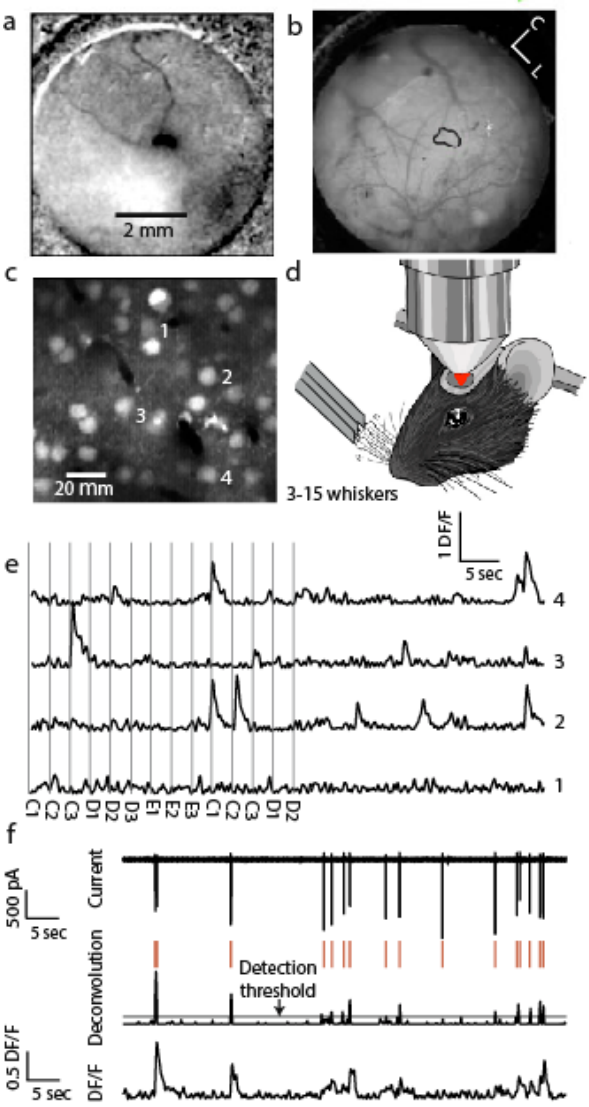

Figure I-1. Ensemble calcium imaging in S1 *in vivo*

(A-B) Intrinsic signal imaging of D2 whisker response area through intact skull, used to target OGB1-AM dye injection. (C) Example imaging field loaded with OGB1-AM. (D) Whisker stimulation during imaging. (E) ΔF/F traces for 4 neurons labeled in (C). Gray lines, individual whisker deflections. Right half of traces show spontaneous activity epoch. (F) Calibration of calcium imaging sensitivity for one neuron. Bottom, ΔF/F trace. Middle, deconvolution output showing instantaneous probability of a Ca^{2+} event, thresholded to yield a calcium event train (red). Top, simultaneous cell-attached recording of spikes. See also Figure S1.

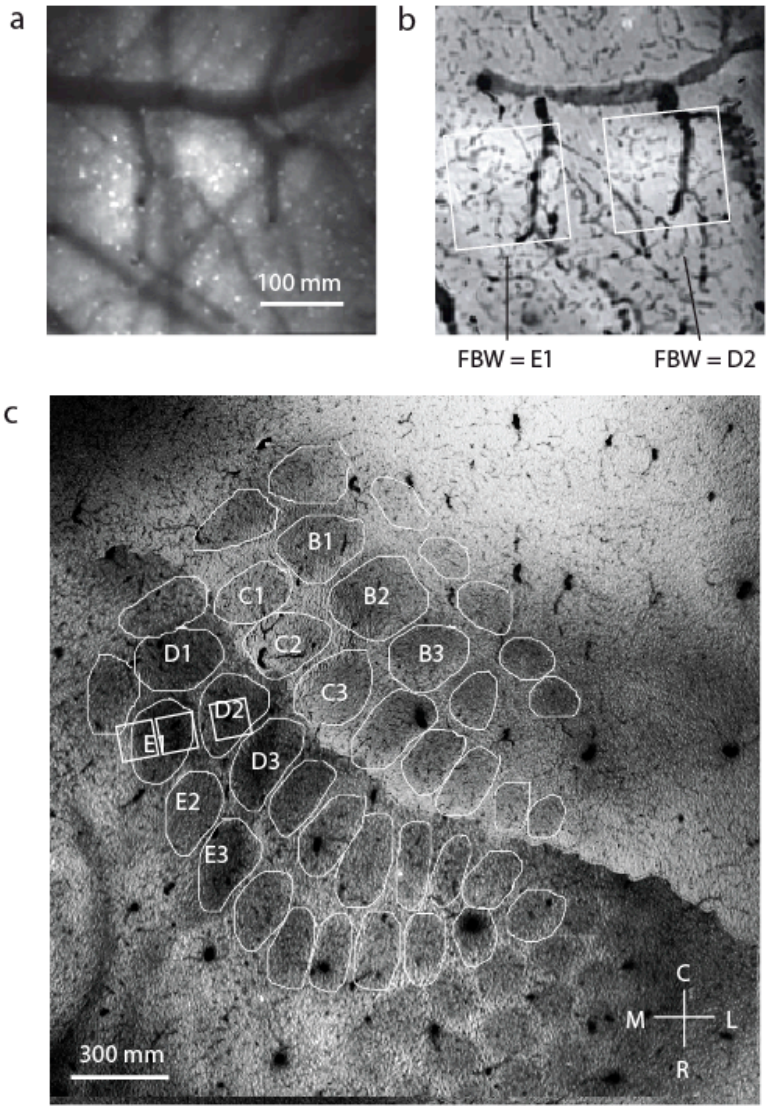

Figure I-2. Anatomical localization of imaging fields, related to Figure 1.
(A) Low magnification 2-photon image of OGB1-AM loaded cortex showing surface blood vessels. (B) The same blood vessel configuration found in a flattened, CO-stained, histological section. Boxes show locations of two imaging fields, with FBW of E1 and D2, respectively. (C) Positions of 3 imaging fields from the same mouse as in (A-B) projected onto the L4 barrel map in CO-stained sections from that animal. The CO image is a montage over several histological sections. Each anatomical barrel is marked with its whisker identity, and the FBW for each imaging field is shown in bold.

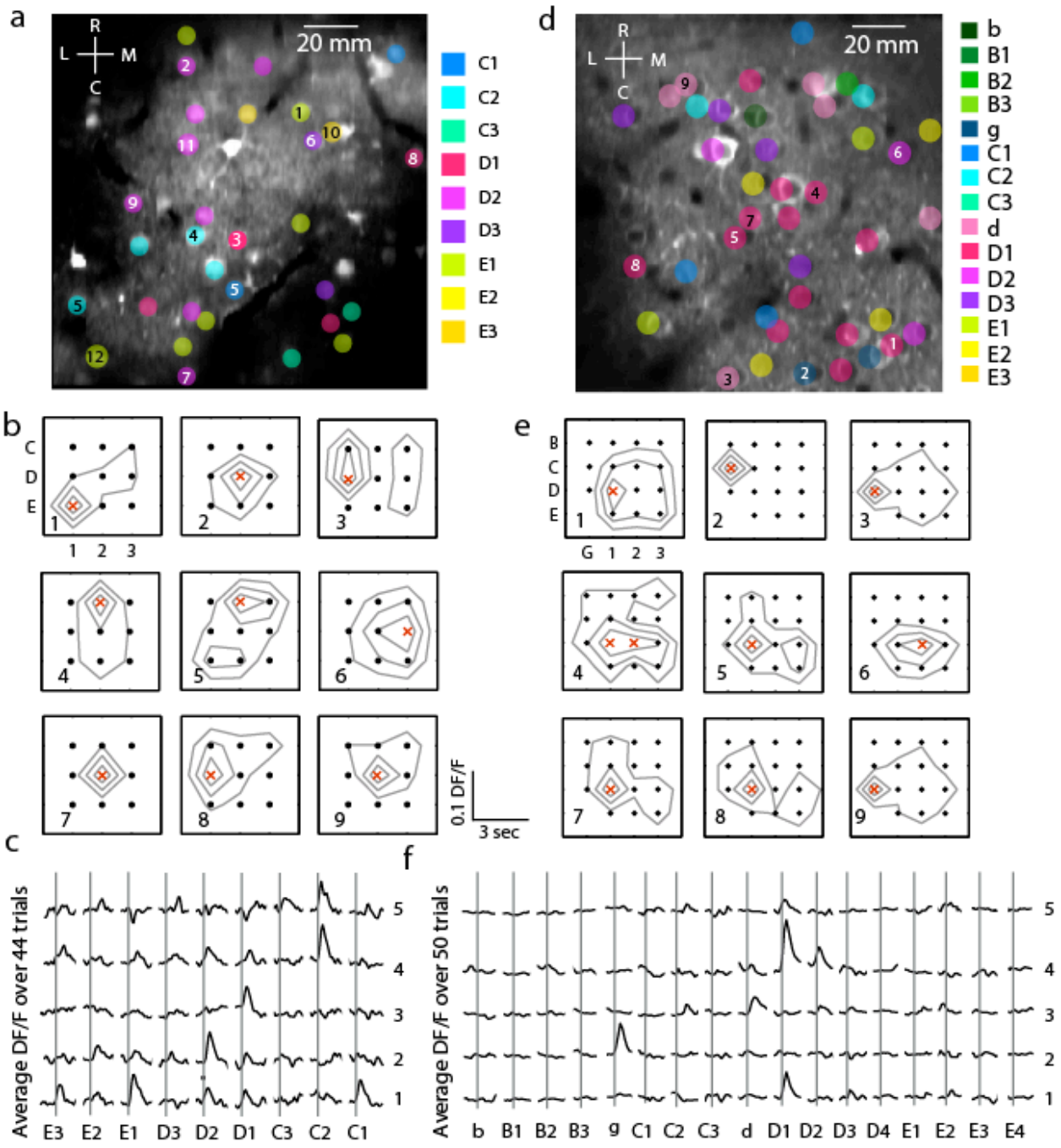

Figure I-3. Heterogeneous whisker tuning among L2 neurons

(A-C) Example imaging field in a D2 barrel column. (A) All neurons, with color indicating PW. (B) Tuning curves for the 9 most responsive neurons. Grey contours denote 25, 50 and 75% of maximum Pr. Crosses mark PW and all whiskers with statistically indistinguishable P_r from the PW. (C) Mean whisker-evoked ΔF/F for 5 most responsive neurons. (D-F) Example field in D1 column imaged with GCaMP6f. Conventions as in (A-C). See also Figure S2.

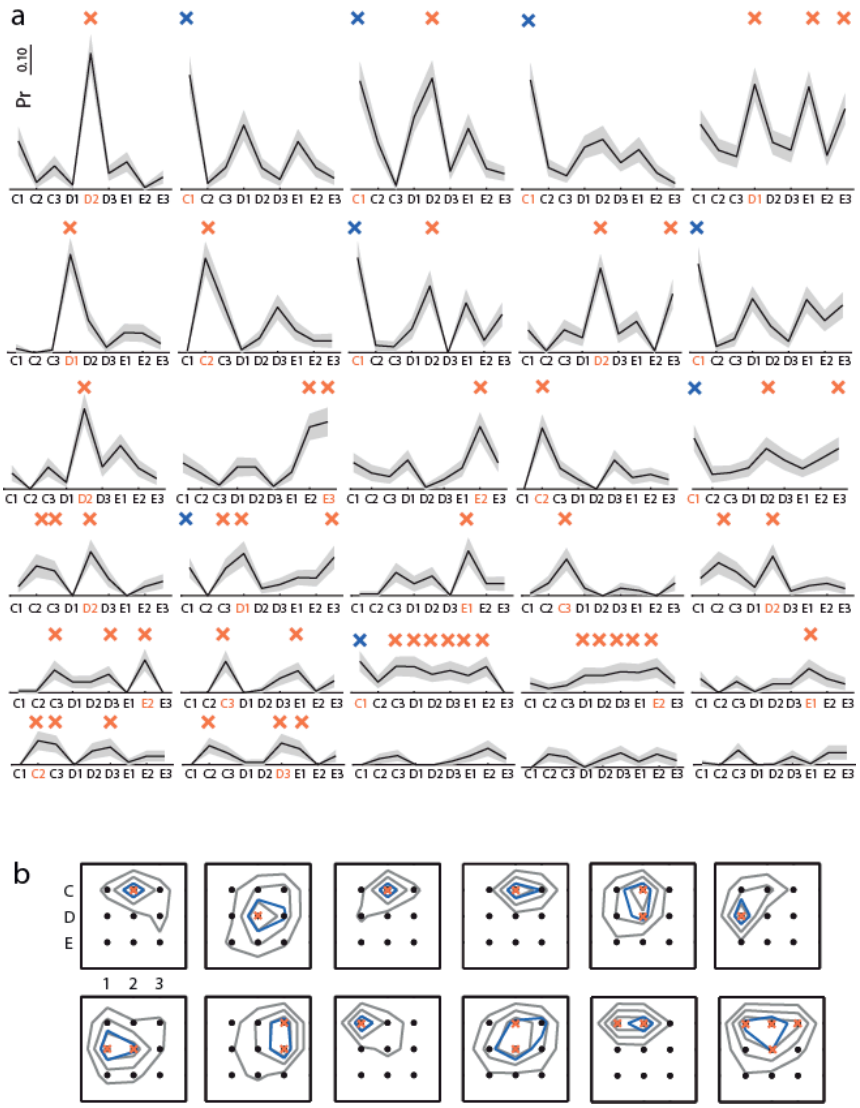

Figure I-4. Heterogeneous whisker tuning in two additional imaging fields

(A) Whisker tuning curves for all neurons in one field. The field best whisker was C1. Shading shows 95% confidence interval for mean P_r, assuming Poisson statistics. X's show all whiskers with P_r statistically indistinguishable from the PW. Blue X's, C1 whisker. The PW for each cell (the whisker that evoked maximum P_r) is shown in red. (B) Whisker tuning for the twelve most responsive cells in another field. The FBW was C2. Grey contours denote 25, 50 and 75% of Pr_{PW}. X's show PW and all other whiskers with statistically indistinguishable P_r. Blue contour encloses whiskers evoking > 75% of maximum peak ΔF/F (without deconvolution). The close agreement of blue and grey contours shows that heterogeneous whisker tuning is not an artifact of the deconvolution method.

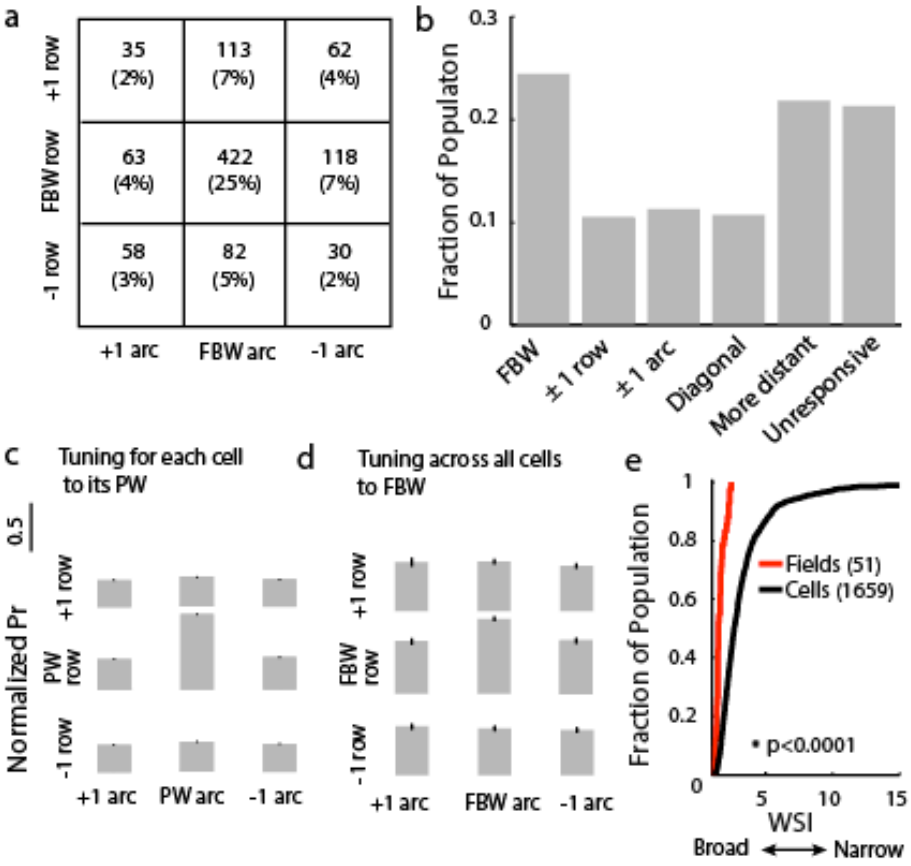

Figure I-5. Quantification of tuning heterogeneity

(A) Number of neurons tuned to different whiskers, across all fields. (B) Fraction of population tuned to different whiskers. (C) Average single-cell tuning curve. Responses were centered around the individual cells' PW and responses normalized to PrPW. Bars show SEM. (D) Average single-field tuning curve (calculated across all cells in a field). Responses were centered around the FBW. (E) WSI for individual cells vs. fields, showing that individual neurons are more narrowly tuned than fields. This analysis only includes cells with $Pr_{PW} \geq 0.05$.

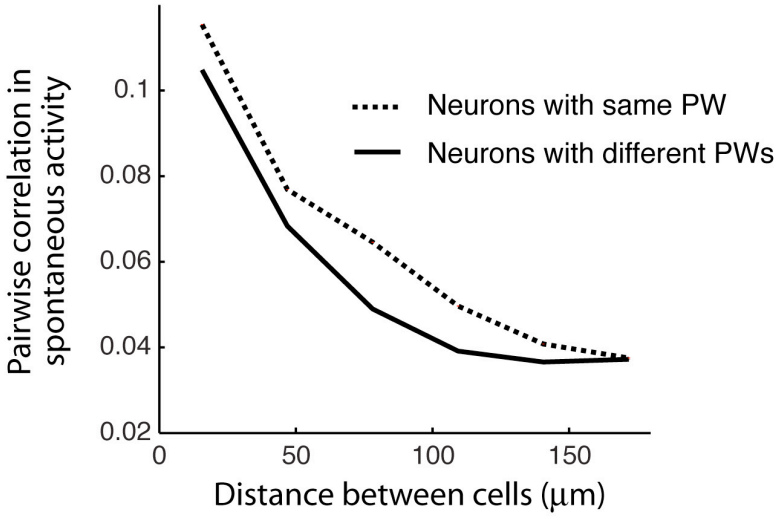

Figure I-6. Co-tuned neurons show correlated spontaneous firing
Mean pair-wise correlation during spontaneous activity periods, for neurons that share the same PW, or neurons with different PWs. Correlation values fell off rapidly with distance between cells. Correlations were greater for co-tuned neurons than differently tuned neurons at distances < 100 mm.

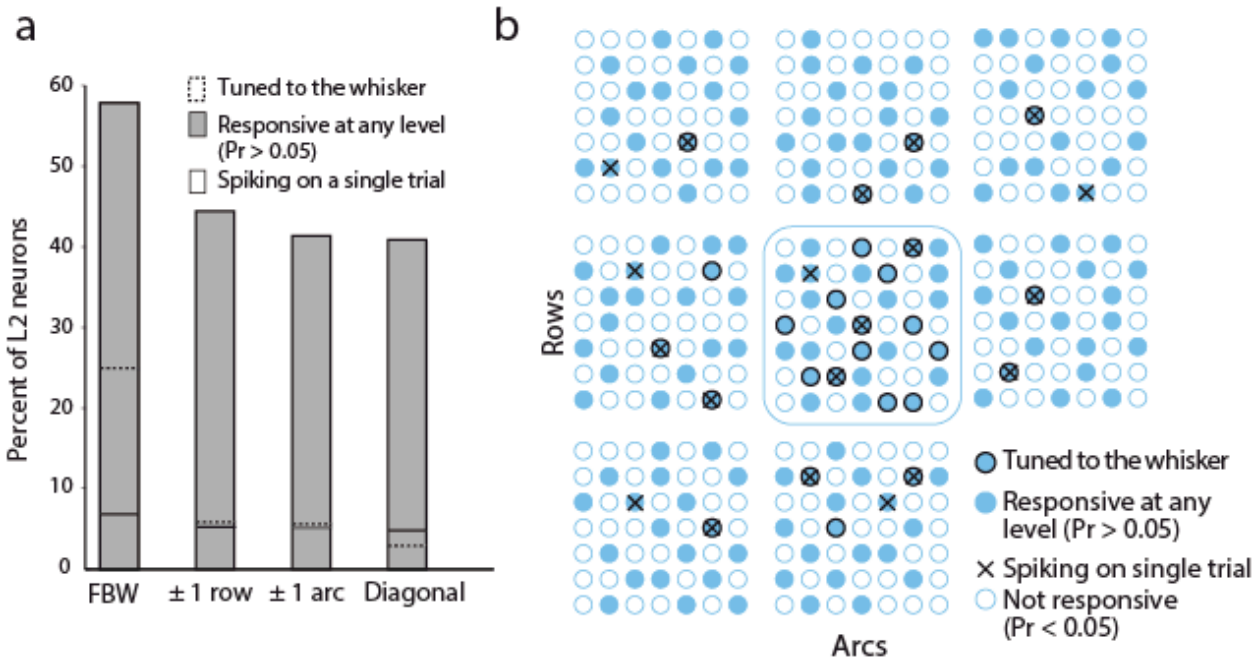

Figure I-7. Point representation of one whisker in L2 of S1

(A) Grey bars indicate the population of neurons in a single column that are minimally responsive to a given whisker (Pr ≥ 0.05). Dotted lines indicate the population that is tuned to a given whisker; black lines indicate the population that spikes to a single whisker deflection. (B) Schematic representation of single whisker deflection in L2 over multiple columns. Deflection of whisker corresponding to outlined barrel column elicits sparse spiking across a large number of columns.

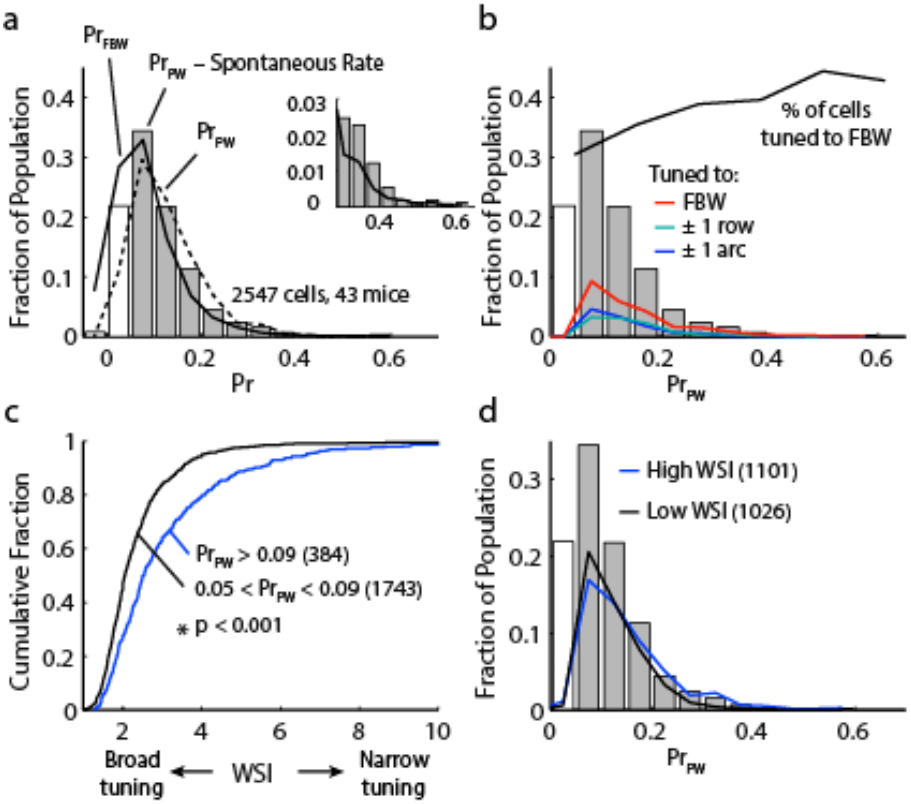

Figure I-8. Effect of column-specific whisker tuning on P_r

(A) P_r distribution across all imaged cells. Black curve, Pr_{FBW} (not corrected for spontaneous firing). Dashed curve, Pr_{PW} (not corrected for spontaneous firing). Histogram bars, Pr_{PW} corrected for spontaneous firing. White bar, unresponsive neurons ($Pr_{PW} \leq 0.05$). Inset shows tail of high-responsive neurons for Pr_{PW} and Pr_{FBW}. (B) Effect of PW identity on Pr_{PW}. Histogram bars show entire population, reproduced from (A). Colored curves show subsets of neurons tuned for FBW or nearby whiskers. Black curve, fraction of cells tuned to FBW as a function of Pr_{PW}. (C) High Pr_{PW} neurons are more narrowly tuned than low Pr_{PW} neurons. (D) Effect of tuning width on PrPW. Histogram, entire population reproduced from (A). Blue and black curves, high-WSI (narrowly tuned) and low-WSI (broadly tuned) neurons.

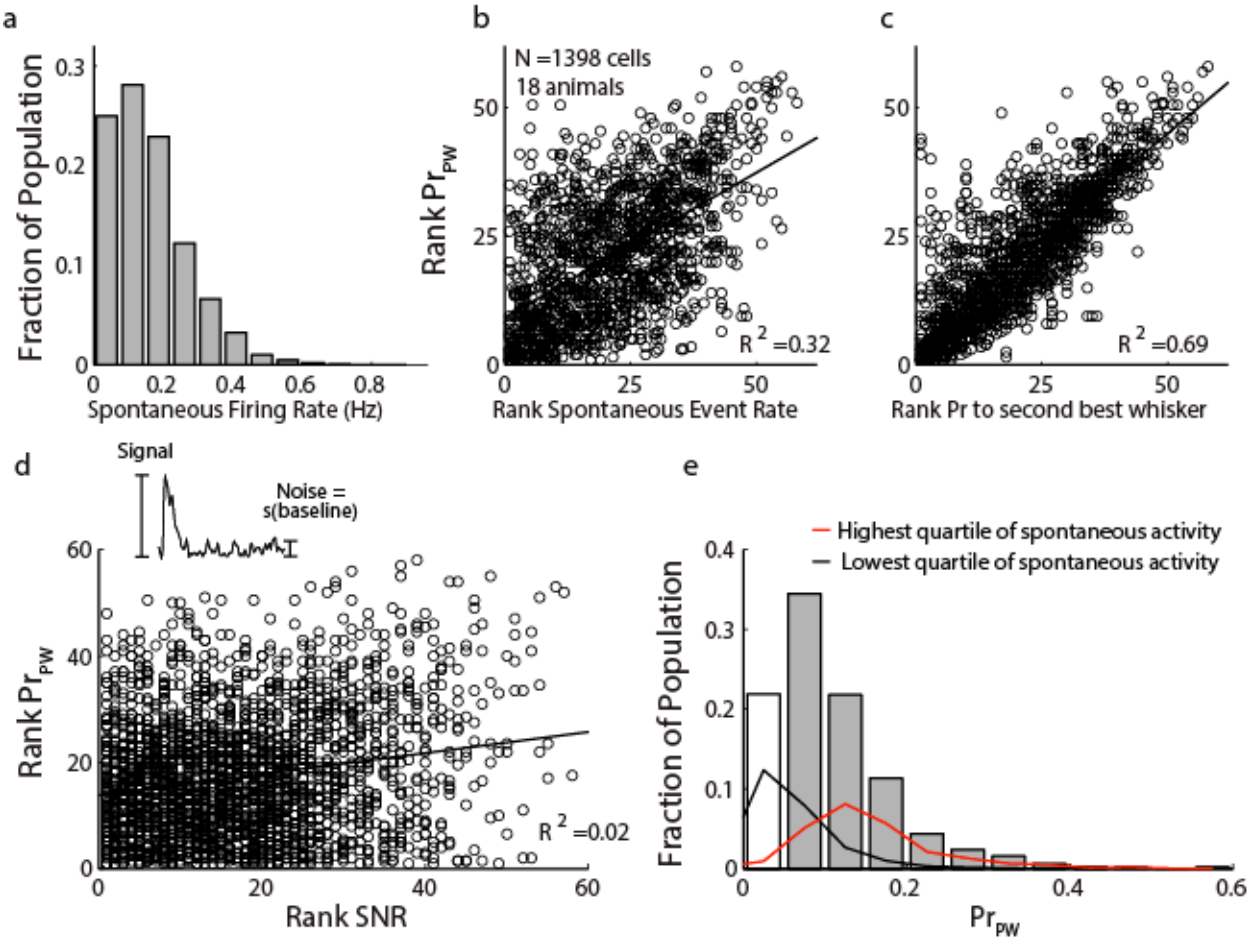

Figure I-9. The whisker-evoked response spectrum correlates with spontaneous activity
(A) Histogram of spontaneous firing rates. (B) Correlation between Pr_{PW} and spontaneous firing rate, calculated by rank within the imaging field for each neuron. Only data from fields with > 30 cells are included to ensure adequate sampling of response properties in each field. (C) Same as (B) but for P_r to each neurons 2nd-best whisker. (D) SNR and Pr_{PW} are not correlated. Inset, SNR calculation. (E) Effect of spontaneous firing rate on Pr_{PW}. Histogram bars show entire population, reproduced from Figure 5A. Black and red curves, neurons with lowest and highest quartile of spontaneous activity. See also Figure S4.

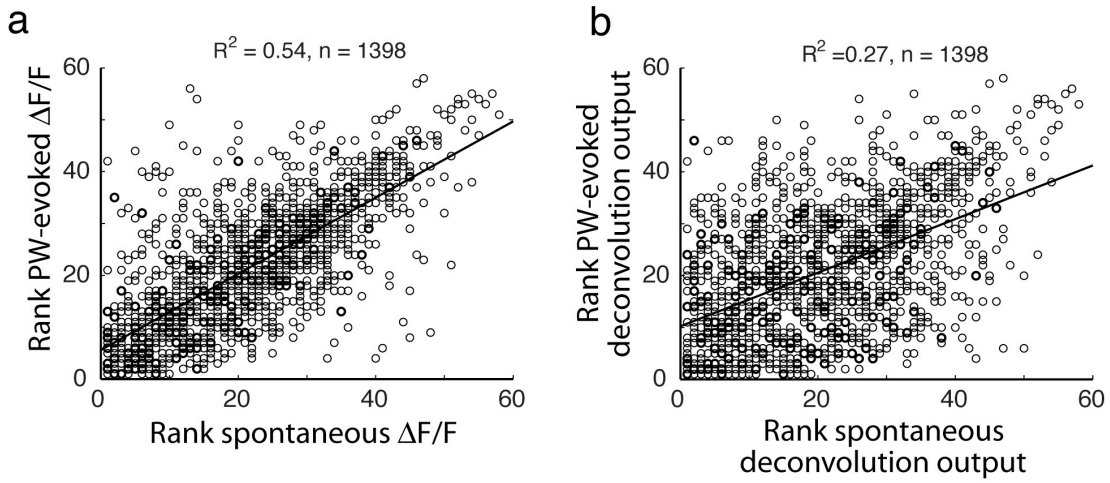

Figure I-10. Further evidence that whisker responsiveness correlates with spontaneous activity.

(A) PW-evoked DF/F amplitude was correlated with DF/F averaged across spontaneous epochs. Correlation was performed on rank DF/F within the imaging field. Only fields with > 30 cells were included. (B) The correlation between PW-evoked P_r and spontaneous P_r does not depend on event thresholding. The panel shows PW-evoked deconvolution algorithm output (without thresholding) vs. average algorithm output across spontaneous epochs. Correlation was performed on rank within the imaging field. Only fields with > 30 cells were included.

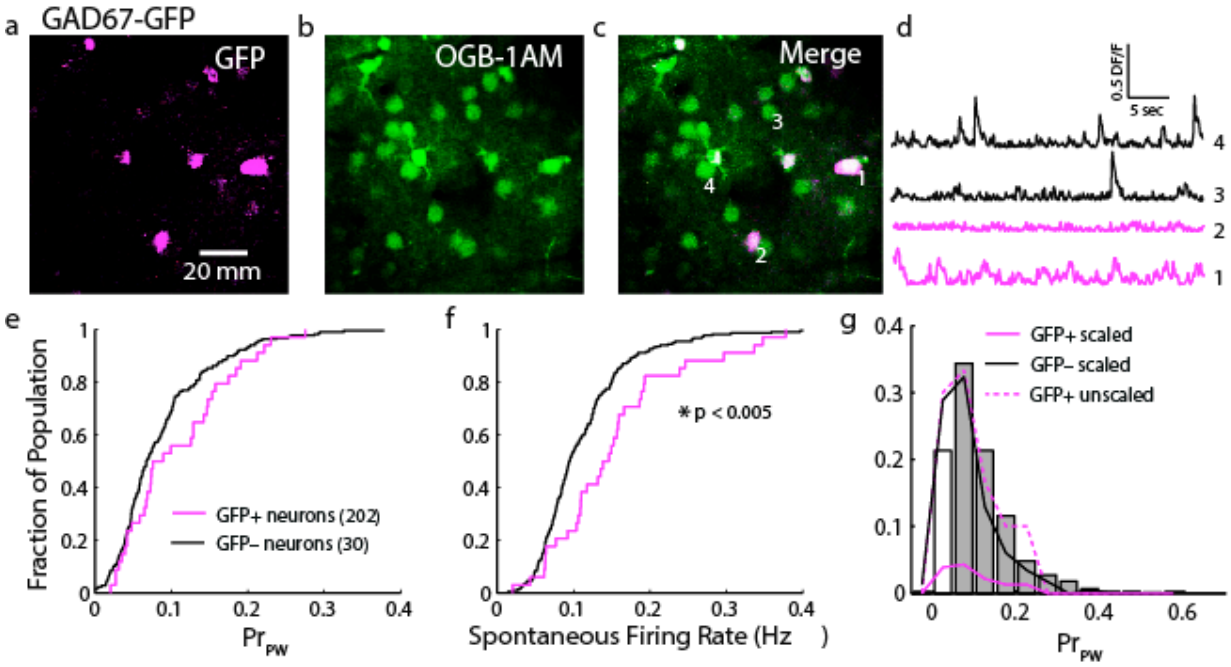

Figure I-11. Responsiveness of interneurons vs. pyramidal cells in GAD67-GFP mice
(A-C) Example imaging field showing GFP-labeled interneurons (A, imaged at 920 nm), OGB-1 dye loading (B, imaged at 800 nm), and (C) the overlay. (D) ΔF/F traces for 4 neurons indicated in (C). Magenta traces are interneurons. (E-F) Cumulative distributions of Pr_{PW} and spontaneous firing rate for interneurons and putative pyramidal cells. (G) Distribution of Pr_{PW} for interneurons and putative pyramidal cells (curves), overlaid on Pr_{PW} for all neurons (bars, replotted from Fig. 5A).

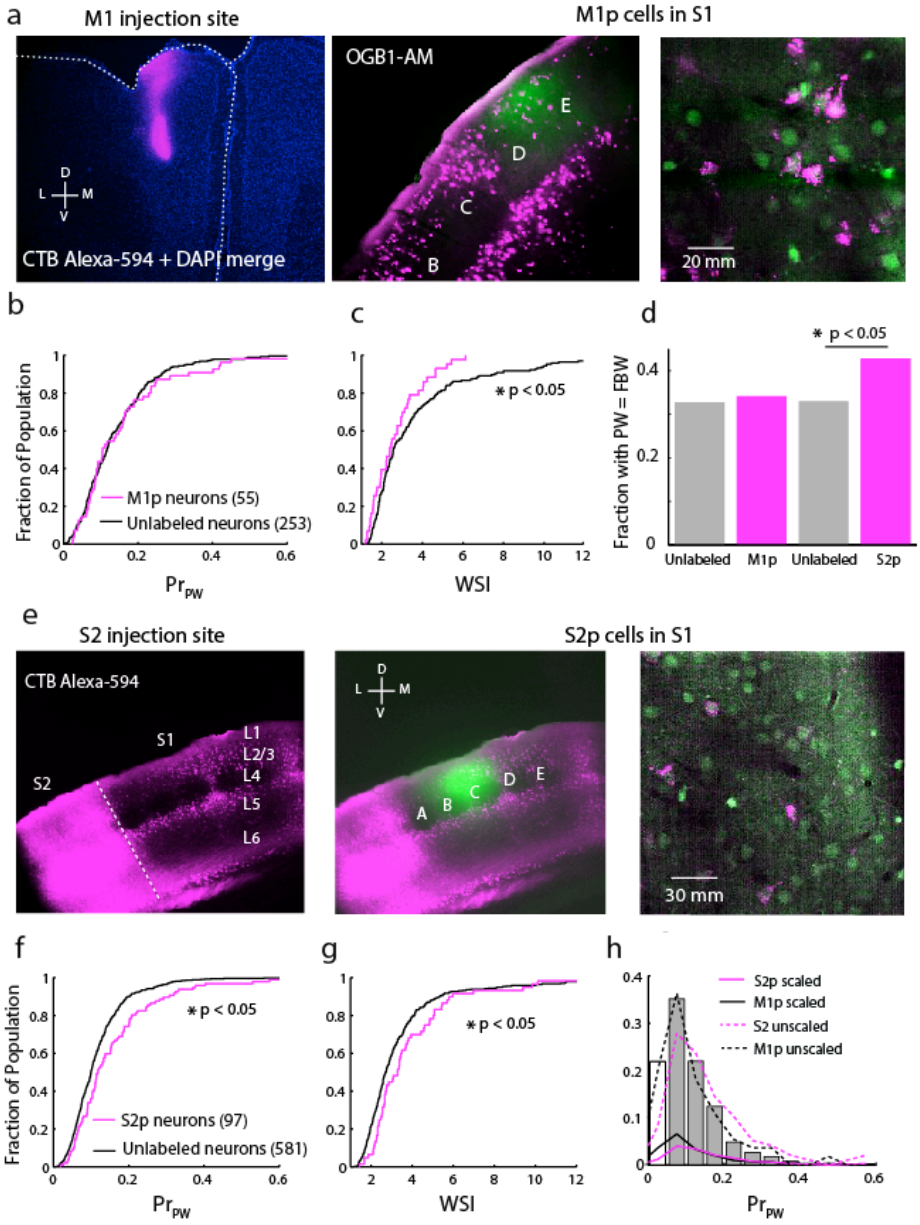

Figure I-12. S2p and M1p pyramidal cells differ in responsiveness and tuning

(A) CTB-Alexa594 injection site in M1 (left) that labeled M1p cells in S1 (magenta cells in middle and right panel, visible among green OGB-1 labeled neurons). Right is an example imaging field in S1. (B-C) Cumulative distributions of Pr_{PW} and WSI for M1p and unlabeled neurons. (D) Fraction of each population that were tuned to the FBW. (E) CTB-Alexa594 injection site in S2, and S2p cells (magenta) in S1. (F-G) Cumulative distributions of Pr_{PW} and WSI for S2p unlabeled neurons. (H) Pr_{PW} distribution for M1p and S2p neurons overlaid on the distribution for all neurons. Bars are reproduced from Fig. 5A. See also Figure S5.

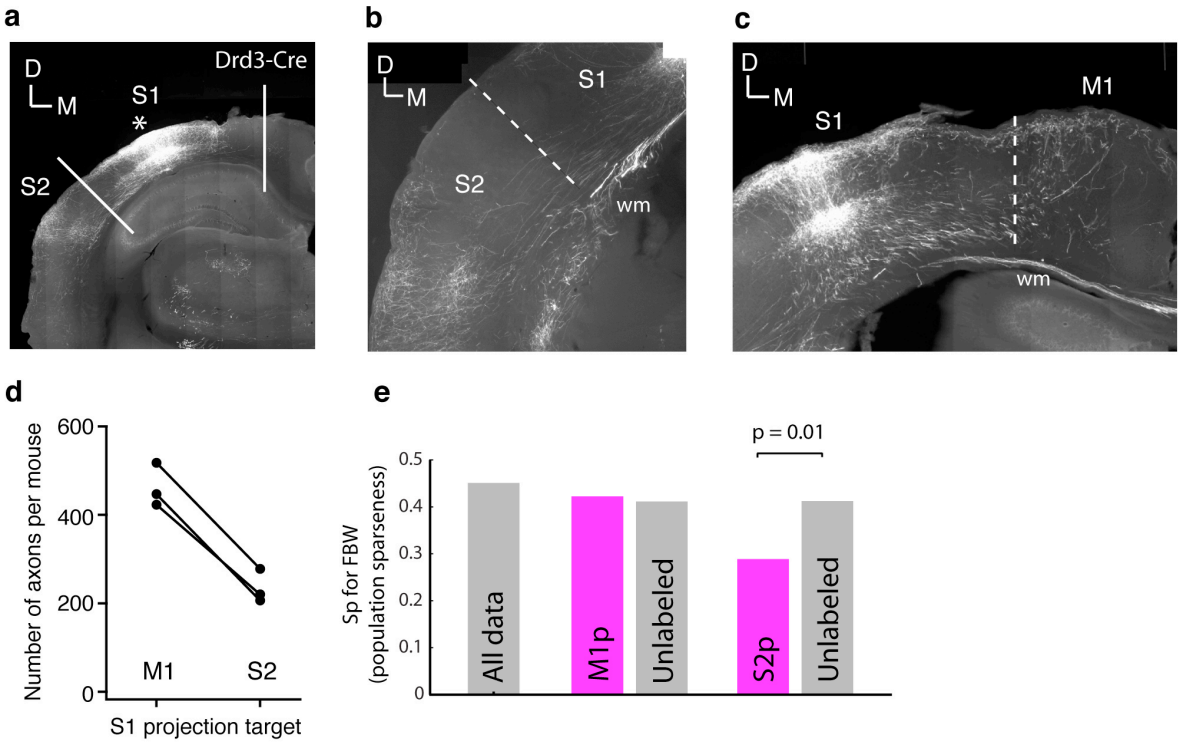

Figure S5. Axon number and coding density in S2p and M1p projections.

Figure I-13. Axon number and coding density in S2p and M1p projections.
(A) AAV2.9-flex-tdTomato injection site (asterisk) in S1 in a Drd3-Cre mouse, showing tdTomato expression in S1 pyramidal cells. 90% of labeled cells were in L2/3, and 10% were in L5. Lines show medial and lateral boundaries of S1. (B) Example section showing tdTomato labeled axons leaving S1 and entering S2. Dashed line, S1-S2 border plane at which crossing axons were counted. Axons traveling in the white matter (wm) were not counted. (C) Example section showing tdTomato labeled axons leaving S1 and entering M1. Dashed line, S1-M1 border plane at which crossing axons were counted. Axons traveling in white matter (wm) were not counted. (D) Quantification of number of S1→M1 and S1→S2 axons (n = 3 mice). (E) Population sparseness (S_p) for FBW-evoked responses among different populations of L2 neurons. 'All data' represents all L2 neurons from Figs. 3-6. The two 'unlabeled' bars denote non-retrogradely labeled neurons in M1p cases and S2p cases, respectively.

II. VOLITIONAL MODULATION OF OPTICALLY RECORDED CALCIUM SIGNALS DURING NEUROPROSTHETIC LEARNING

Introduction

Brain-machine interfaces (BMIs) have gained great momentum as a therapeutic option for patients with limb loss or immobility (Carmena et al., 2003; Hochberg et al., 2012; Nicolelis, 2001; Wodlinger et al., 2013). In addition, BMI tasks provide a powerful approach to study sensorimotor learning, as they enable arbitrary mapping between neuronal activity, behavioral output, and reward (Green and Kalaska, 2011). Recent work used BMI to demonstrate network adaptations in response to output perturbations (Jarosiewicz et al., 2008), including specific functional changes in output-relevant neurons (Ganguly et al., 2011; Koralek et al., 2013). However, traditional BMIs based on spatially sparse electrode recordings lack fine-scale spatial information about local networks. To address this issue, we developed a BMI task in awake, head-restrained mice using 2-photon calcium imaging to record activity from every neuron in a small field of view (150 by 150 microns). We used this novel calcium-based BMI paradigm (CaBMI) to probe fine-scale network reorganization in cortical layer (L) 2/3 of both primary motor (M1) and somatosensory (S1) cortices during BMI learning.

Results

We trained ten mice expressing the genetically-encoded calcium indicator gCaMP6f in L2/3 of M1 or S1 to modulate neural activity in response to auditory feedback (Figure II-1a, Methods). This task was adapted from one used previously with electrode-based recordings (Koralek et al., 2012). Each day, two ensembles containing 1-11 neurons each were chosen to control the task (Figure II-2a). The ensembles opposed each other, such that increased activity in one ensemble ("E1") above its baseline increased the pitch of the auditory feedback, while increased activity in the other ensemble ("E2") decreased the pitch. Reward was delivered when a high-pitched target was reached within 30 sec of trial initiation (hit). Incorrect trials (no target within 30 s) were signaled with white noise.

Mice learned the task rapidly (Figure II-2b), with initial rapid improvement (1-3 days) followed by slower improvement (4-8 days). Mice performed above chance level after 1 day of training (Figure II-2b, shaded region, N=10 mice, p=0.0036 on day 2, t (8)=4.07). Similar learning occurred using M1 or, more surprisingly, S1 (Figure II-1 b-c). Hit rate increased significantly within each daily session (Figure II-1d, N=72 sessions, 10 mice, $p=2.6x10^{-5}$, t (43)=4.7, $R^2=0.34$). Mice reached a criterion performance level (50% hits) faster across days of training (Figure II-1e, N=8 days, 10 mice, p=0.0247, t (6)=2.98, $R^2=0.596$), suggesting that within-session learning occurs faster as between-session learning progresses. As seen previously (Koralek et al., 2012), performance was not impaired by lidocaine injection into the contralateral mystacial pad (N = 4 mice, p=0.876, t (3)=0.17), and gross movements were absent preceding target hits, indicating that performance does not rely on natural movement and that neural activity, particularly in S1, is not driven by whisker reafference (Figure II-3).

We next asked whether these modulations were sensitive to the action-outcome contingency (Hilario et al., 2007). After mice successfully learned the task, we ceased rewarding target hits and instead delivered rewards under a variable interval schedule (contingency

degradation). Mice quickly ceased responding (Figure II-2c-d; N=5 mice, p=0.0089, t (4)=4.76). When reward was reinstated using the same E1 and E2 ensembles, mice again performed at normal levels (Figure II-2c; N=4 mice, p=0.791, t (3)=0.289). Thus, performance was sensitive to reward contingency, suggesting the behavior is goal-directed (Dias-Ferreira et al., 2009). Post-hoc analysis of imaging data showed that E1 activity increased during task performance and decreased during degradation (Figure II-2d, Figure II-4a). On a separate day, we performed a contingency reversal (N=3 mice) in which E1 and E2 identities were reversed from one day (day CR1) to the next (day CR2), requiring mice to reverse ensemble activity patterns to obtain reward (Figure II-5a). Early during CR2, E2 in one example mouse showed clear bursting activity (consistent with its identity as E1 on CR1), and E1 showed little activity (consistent with its identity as E2 on CR1). This pattern quickly reversed as the mouse learned the new contingency (Figure II-5a). We compared the hit rate on CR2 in one animal to a simulated hit rate based on the E1/E2 identity and transform algorithm from day CR1. The simulation showed initially high performance that then dropped to zero, indicating that this mouse initially performed according to the learned CR1 transform, but quickly adapted to the new CR2 transform (Figure II-2e). Across all mice, the ratio of E1/E2 activity increased during CR2 (Figure II-5b), demonstrating that mice learn to flexibly up-modulate E1 over E2. Together, these data indicate that mice can modulate calcium signals in a contingency-dependent manner, and that these modulations can be applied to arbitrarily chosen cells.

We next investigated neural changes during learning. Mean DF/F increased for E1 cells over the course of individual sessions (Figure II-4a; N=20 time points, 10 mice, $p=1.17\text{x}10^{-11}$, t (18)=15.09, R^2=0.927), decreased during subsequent contingency degradation (Figure II-6a; N=20 time points, 5 mice, p=0.0029, t (18)=-3.44). In contrast, mean DF/F did not significantly change for E2 cells (Figure II-6b, c; p=0.234, p=0.13, respectively). This may reflect a bias toward volitional increases, rather than decreases, of L2/3 activity.

Calcium imaging detects activity even in neurons that are rarely active, which are numerous in L2/3 (Barth and Poulet, 2012; O'Connor et al., 2010b). These cells are undersampled by extracellular recordings and are often neglected in BMI studies (Shoham et al., 2006). There was a 30-fold range of baseline spontaneous activity across L2/3 cells (Fig. II-4b). We found the most dramatic increases in task-related activity in E1 cells with initially low baseline (Figure II-4b, t-test of low vs. more-active E1 cells, N=72 cells, p=8.05e-8, t (70)=5.99). Low-baseline E2 cells tended to decrease their activity during task-engagement slightly more than high-baseline cells (Figure II-4b, t-test of low vs. more-active E2 cells, N=78 cells, p=0.02, t (76)=-2.37), though mean activity remained unchanged (Figure II-6b). Thus, task learning preferentially recruited low-active E1 neurons to become more active. These neurons clearly contributed to learning, because learning occurred normally when all E1 cells had low or zero baseline activity (Figure II-7a, N=46 sessions, 10 mice, p=0.83, t (44)=1.56), suggesting a role for "silent" L2/3 neurons in learning (Barth and Poulet, 2012). We also found that within multi-cell E1 ensembles, multiple cells increased fluorescence around hits, including low- and zero-baseline cells, and so performance was not carried by single neurons (Figure II-7b).

To examine higher-level network dynamics during learning, we first calculated mean cross-correlation histograms time-locked to the occurrence of large fluorescence events in either E1 or E2 ("output cells"; Methods). Output cells developed coordinated, synchronous activity with other cells in the same ensemble (Figure II-4c,d). E2 also developed a tendency to

spike before E1 (Figure II-4c, d), likely reflecting a strategy of bursting E2 for trial initiation, followed by bursting of E1 for target achievement. This coordinated activity was not present in non-output cells that were simultaneously imaged (Figure II-4c,d; "indirect cells"). This prompted us to investigate correlations between cells over the course of individual sessions. Correlations between output cells in the same ensemble increased significantly during the session (N=5 time points, 10 mice, p=0.0198, t (3)=4.55, R^2=0.874), while correlations between indirect cells did not (Figure II-4e; N=5 time points, 10 mice, p=0.138, t (3)=2.01), and this enhancement was observable in individual animals (Figure II-8a). Output cells also became more correlated over days of training, even though neural composition of ensembles changed (Figure II-8b N=8 days, 10 mice, p=0.011, t (6)=3.59). This is analogous to increased correlations of functionally-related cells during motor learning (Komiyama et al., 2010) and could reflect millisecond-precision coupling that has been demonstrated with electrodes (Ben Engelhard et al., 2013).

We next examined how fine-scale (~10-100 microns) spatial organization of ensembles impacted learning. Performance did not vary systematically with distance between output ensembles (measured by E1 and E2 centroids) (N=71 sessions, 10 mice, p=0.95, t (69)=0.056), but did vary with size of ensembles: animals performed better with fewer neurons, suggesting that it was difficult to maintain coordinated control over large ensembles (Figure II-9). Additionally, high baseline correlations between ensembles predicted worse performance (Figure II-10).

Learning was accompanied by interesting dynamics within local networks surrounding the output ensembles. For each indirect cell, we calculated the correlation between its mean fluorescence and a moving average of the animal's instantaneous hit rate. We found that activity in indirect cells near E1 (<50 μm away) was significantly more correlated with hits than activity in distant indirect cells (>100 μm away; Figure II-4f, N=251 cells, 10 mice, p=0.048, t (249)=1.98). Finally, we calculated mean target-related modulations in indirect cells for early and late epochs within daily sessions. Early in sessions, indirect cells increased DF/F around hits compared to late in sessions (Figure II-4g, t-test early vs. late modulations, 437 cells, 5 mice, p=3.94e-4, t (436)=3.57). This was evident in cells close to E1 compared to distant cells (t-test early vs. late modulations in close cells, 172 cells, 5 mice, p=0.001, t (171)=3.32; t-test early vs. late modulations in distant cells, 265 cells, 5 mice, p=0.08, t (264)=1.72). Thus, early in the session mice up-modulate activity in a local network surrounding E1 cells (Ganguly et al., 2011), but as the session progresses this target-related modulation in indirect cells disappears, such that mainly output cells exhibited task-related increases in activity. This suggests that mice are able to hone in on individual output cells during learning and precisely modulate these cells for efficient target achievement. Even late in sessions, indirect neurons that were more highly spontaneously correlated with E1 cells, and therefore more likely to be embedded in the same local sub-network (Harris and Mrsic-Flogel, 2013), exhibited increased activity during task engagement compared to cells with low spontaneous correlations with E1 (Figure II-11a; N=851 cells, 10 mice, p = 2.35e-5, t (849)=4.26). Indirect neurons that were more highly spontaneously correlated with E2 cells exhibited decreased activity during task engagement compared to cells with low spontaneous correlations with E2 (Figure II-11b; N=851 cells, p = 0.015, t (849)=-2.6). Given the rapid falloff of spontaneous correlations with distance, such fine-scale effects might be undetectable by electrode-based methods (Figure II-11c). This spatial restriction in activity is

similar to sparsening of cortical representations during classical conditioning (Gdalyahu et al., 2012).

To the best of our knowledge, our results represent the first demonstration that mice can volitionally modulate calcium dynamics in L2/3 of M1 and S1, and the use of imaging enabled dissection of learning-related network modifications during BMI with unprecedented spatial resolution (~10-100 μm). Importantly, this novel paradigm provides a powerful tool for investigating the spatial extent of functional and structural plasticity during neuroprosthetic learning.

Methods

All animal procedures were performed in accordance with UC Berkeley Animal Care and Use Committee regulations. 6 C57BL/6J and 4 CD1 male wild-type mice were used in these experiments, ranging in age from postnatal day 30-45. Animals were housed with a 12h dark – 12h light reversed light cycle. All behavioral tests were performed in the same cohort of animals.

Surgery

Mice were anesthetized using isoflurane (2% vol isoflurane/vol O2) and placed in a stereotaxic apparatus. Body temperature was maintained at 37°C using a feedback-controlled heating pad (FHC, 40-90-8D) and a small incision was made in the scalp. The skull was cleaned and a steel headplate was affixed over M1 (1 mm rostral, 1 mm lateral to Bregma) or S1 (1 mm caudal, 3 mm lateral to Bregma) using Metabond dental cement (Parkell, S380). A 3 mm craniotomy was opened over M1 or S1, and 200 nL of AAV2.9 Syn.GCamp6f.WPRE.SV40 (Chen et al., 2013b) (University of Pennsylvania Vector Core) was injected 250 µm below the pia using a Nanoliter 2000 injector (World Precision Instruments). The tracer was delivered using a pulled glass pipette (tip diameter 40-60 µm) at a rate of 40 nL/minute. The pipette was left in the brain for 10 minutes after completion of the injection to prevent backflow. After the pipette was removed, the brain was covered with silicone oil (Sigma product # 181138) and a glass coverslip was affixed to the skull with dental cement, as previously described (Holtmaat et al., 2012). We allowed 2 weeks for recovery and gCaMP6f expression.

Two-Photon Imaging

In vivo imaging was performed with a Moveable Objective Microscope (Sutter) using a Chameleon Ultra Ti:Sapphire mode-locked laser (Coherent, Santa Clara CA) tuned to 900 nm. Photons were collected with a Hamamatsu photomultiplier tube (H10770PA-40) using a Nikon objective (16x, 0.8 NA). Animals were head-fixed on a custom-made spring mounted imaging platform and placed under the 2p microscope. This setup allowed them to run freely, and their movements were recorded by an accelerometer fixed to the underside of the platform. Frames of 128x512 pixels (~160 x 160 mm) were collected at 7.23 Hz using ScanImage software (Pologruto et al., 2003) at 130-180 µm below the pia. The same imaging fields were used every day, localized by landmarks in the surface blood vessels. Imaged fields were stable over the course of training, and because the cortex was stabilized by a snugly fitting coverslip, only severe movements caused motion artifacts. Motion correction for slow drift in the imaging field was performed manually. Any period of gross movement during the task that caused cells to move out of their ROIs resulted in poor task performance, as DF/F of E1 was reduced. In this sense, mice were punished for excessive movement and seem to have learned to remain still during the task (Figure II-4c).

Behavioral Task

Two ensembles of 1-11 single cells each were chosen for inclusion in the “output” population. Cells with bright nuclei, indicating over-expression, were excluded, as were cells with many, poorly separable calcium events, an activity pattern indicative of fast-spiking interneurons. No other selection criteria were used to partition the recorded cells into each ensemble. We also

ensured that many cells with good signal were included in the indirect population to enable a proper comparison. The cells assigned to the output population were changed on some days.

Ensemble activity was measured as mean DF/F for all component neurons. Fluorescence values from these ensembles were binned in 200 millisecond bins and entered into an online transform algorithm that related neural activity to the pitch of an auditory cursor. By modulating activity in these ensembles, rodents controlled the pitch of the cursor. The modulations that we required of the mice were calibrated daily based on a baseline recording session of roughly 2 minutes. Next, 10-15 minutes of spontaneous baseline activity was recorded to assess chance levels of performance. Fluorescence values were smoothed by a moving average of the past 3 time points. Changes in the frequency of the auditory cursor were binned in quarter-octave intervals to match rodent psychophysical discrimination thresholds (Han et al., 2007). Mice then had to modulate calcium dynamics in these neuronal ensembles to move the cursor to a high-pitched target tone that was associated with a 10% sucrose solution reward. A trial was marked incorrect if a target was not achieved within 30 seconds of trial initiation. A trial was self-initiated when E1 and E2 activity returned to baseline levels (either by decreased activity in E1 or increased activity in E2), which reset the tone to its starting pitch. Chance levels of performance (grey shaded region in Figure II-1 b & c, Figure II-2b) were determined by running the animal on the task without reward or auditory feedback. Hits resulted when spontaneous fluctuations were large enough push the decoder to the target frequency. Failure to hit a target in 30 seconds resulted in a miss. The chance region represents the mean chance performance and s.e.m., pooled over all animals and all days.
Regions of interest (ROIs) were extracted from recorded neural data in real time. These ROIs were entered into custom routines in MATLAB (Mathworks, Natick, MA) that translated fluorescence levels into the appropriate feedback pitch and played the pitch on speakers mounted on 2 sides of the imaging platform. Frequencies used for auditory feedback ranged from 1-24 kHz in quarter-octave increments. When a target was hit, a MATLAB-controlled Data Acquisition board (National Instruments, Austin, TX) triggered the operant box to supply the appropriate reward to rodents. Each daily training session lasted 48±2 min (71±4 trials).

Data Analysis
All analyses were performed with custom written routines in MATLAB (Mathworks, Natick, MA). Recorded movies were spatially aligned using the dftregistration routine in MATLAB (Guizar-Sicairos et al., 2008). Regions of interest were manually selected to include the soma of neurons that appeared consistently throughout all recorded movies. Fluorescence traces were extracted from each ROI and data is presented as the relative change in fluorescence, $\Delta F/F$.
No statistical methods were used to pre-determine sample sizes but our sample sizes are similar to those generally employed in the field.
For analyses of behavioral performance during the contingency degradation (Fig 1c), the first 10 trials of a session were removed before calculating performance to exclude the transition period and reflect the animal's performance once the animal had fully learned the new reward contingency.
For all sliding window analyses, sessions were divided into an equal number of bins to determine the window size, and the step size was a fraction of this window size.

For the data plotted in Figure II-4g, mean z-score values during task engagement were binned by distance from E1 or E2 centroid. The first bin included all cells from 0-50 mm from the centroid of the output ensemble ("close" cells), the second bin included all cells 50-100 mm from the output ensemble, and the final bin including all cells 100+ mm from the output ensemble. "Distant" cells included all cells at a distance of greater than 50 mm from the E1 centroid. We include data from 3 days late in training from 5 animals where 20 or more indirect cells were apparent in the field.

For the cross-correlation histograms, fluorescence traces from output cells were z-scored and values above 3 standard deviations were considered an event. The first time point in which fluorescence values crossed this threshold during each event was used for time-locking. Fluorescence values in other populations of cells were then averaged around these indices.

In all cases, multiple comparisons were controlled for using the Bonferroni correction. Differences between groups were tested with T-tests. To evaluate trends over time, we tested whether the slope of a fitted linear regression was significantly different from zero. All statistical tests were two-tailed.

For testing the activity modulations for low vs. more-active cell groups in Figure II-4b, the high active group included cells with spontaneous event rate greater than the median spontaneous event rate, the low active group included cells with spontaneous event rate less than the median.

Data distributions were assumed to be normal, but this was not formally tested. Data collection and analysis were not performed blind to the experimental conditions. Randomization was not performed, as the experiment primarily involved within-animal comparisons and there were not multiple experimental cohorts.

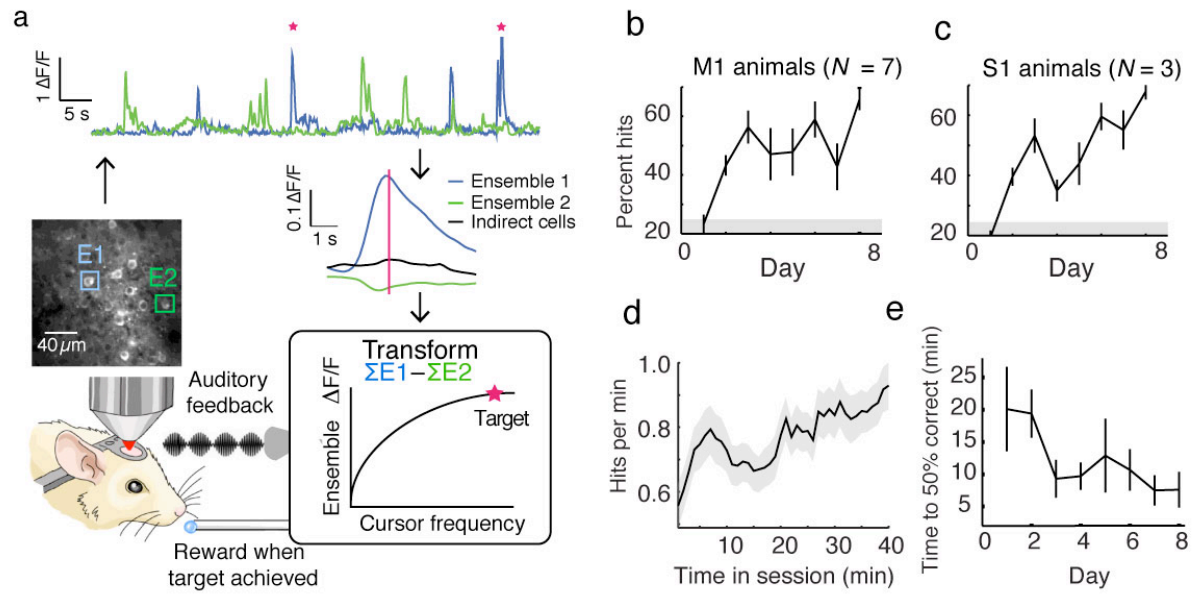

Figure II-1. Mice rapidly learn to intentionally modulate calcium dynamics. a. Task schematic. **b & c.** Behavioral performance over 8 days for animals trained to use M1 (**b**) and S1 (**c**). **d.** Hit rate increases over the course of individual sessions. Shaded region denotes s.e.m., 10 mice. **e.** Animals achieve a criterion performance of 50% hits faster over the course of training. N=8 days, 10 mice

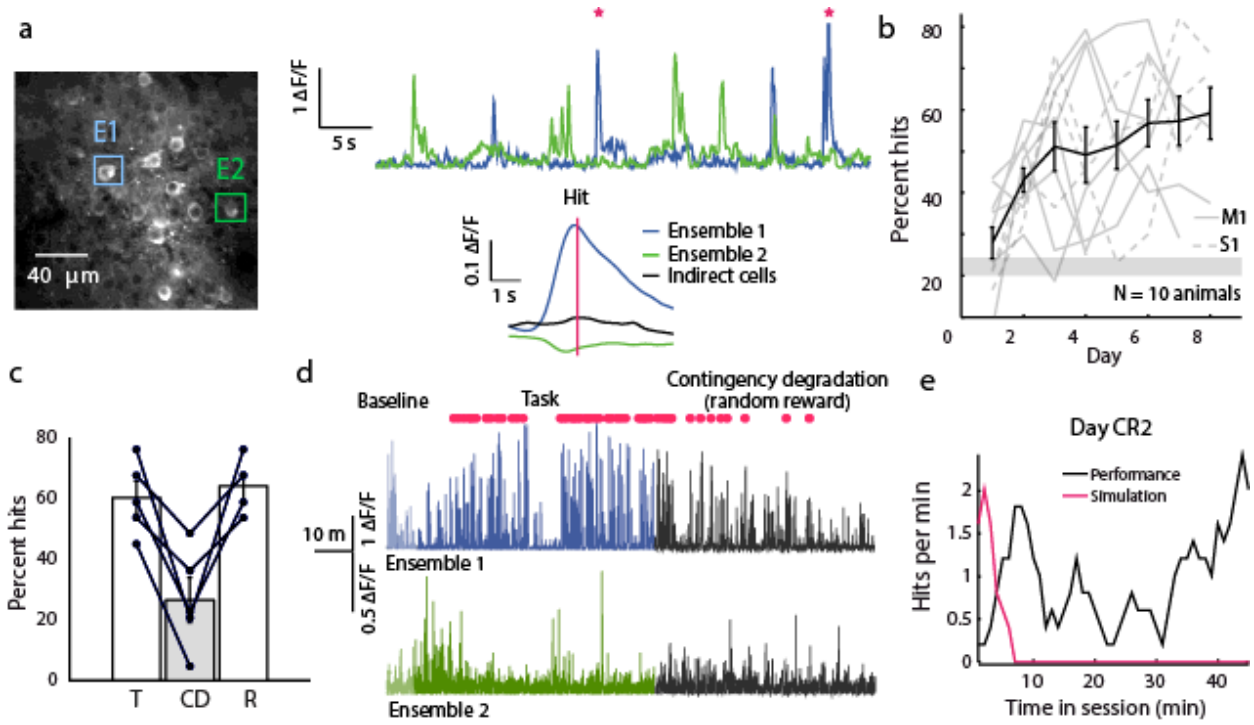

Figure II-2. Mice learn to intentionally modulate calcium dynamics. a. Example imaging field (left) and recordings from cells in E1 and E2 (top right). Red stars indicate hits. Bottom right, mean ensemble fluorescence around hits. **b.** Performance over 8 days of training. Mean performance is shown in black, individual animals in gray. Error bars denote s.e.m. Shaded region denotes chance performance. **c.** Performance rapidly dropped compared to normal task levels (T) during the contingency degradation (CD). Performance returned to previous levels during reinstatement (R). **d.** E1 DF/F increases during the task and decreases during CD. Likewise, target hits (red) increase in frequency over training, and decrease during CD. **e.** At the beginning of day CR2, the animal initially performs as if the previous day's transform algorithm were still in use, but quickly learns the new transform.

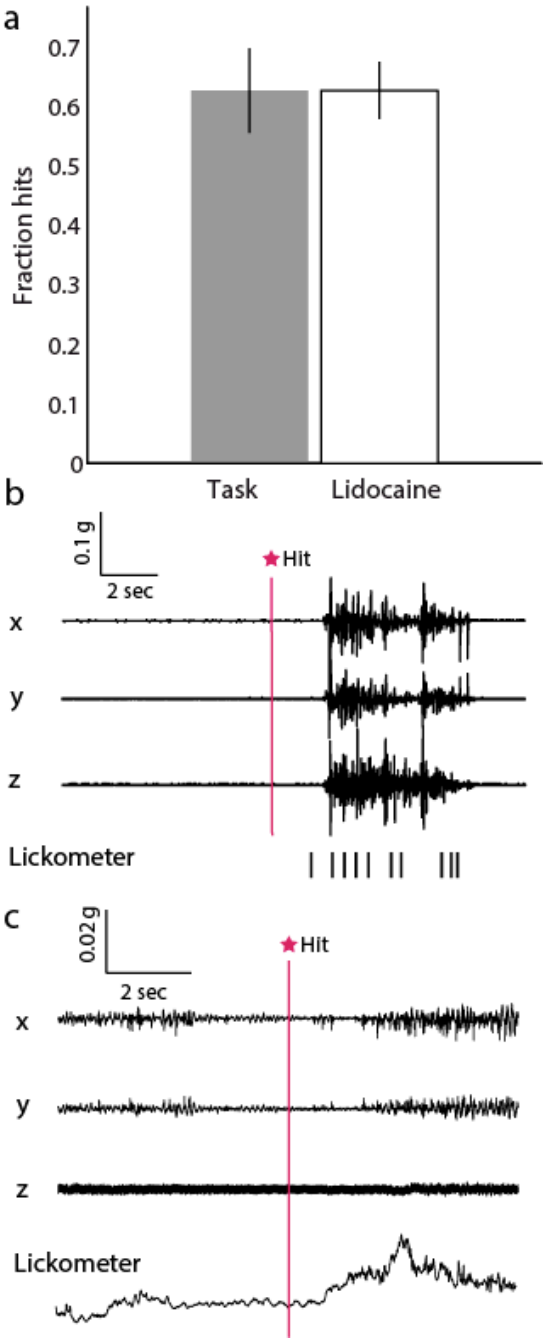

Figure II-3. Task performance does not rely on natural movements. a. Performance on the task was not impaired when we injected lidocaine into the mystacial pad to block whisker movements and somatosensory input. Error bars denote s.e.m. **b.** Accelerometer traces for a single trial with no motion or licking behavior before target achievement, despite clear activity afterwards as mice consume the reward. **c.** Hit-locked accelerometer traces averaged over one entire training session for one animal shows animal does not rely on systematic motion for task.

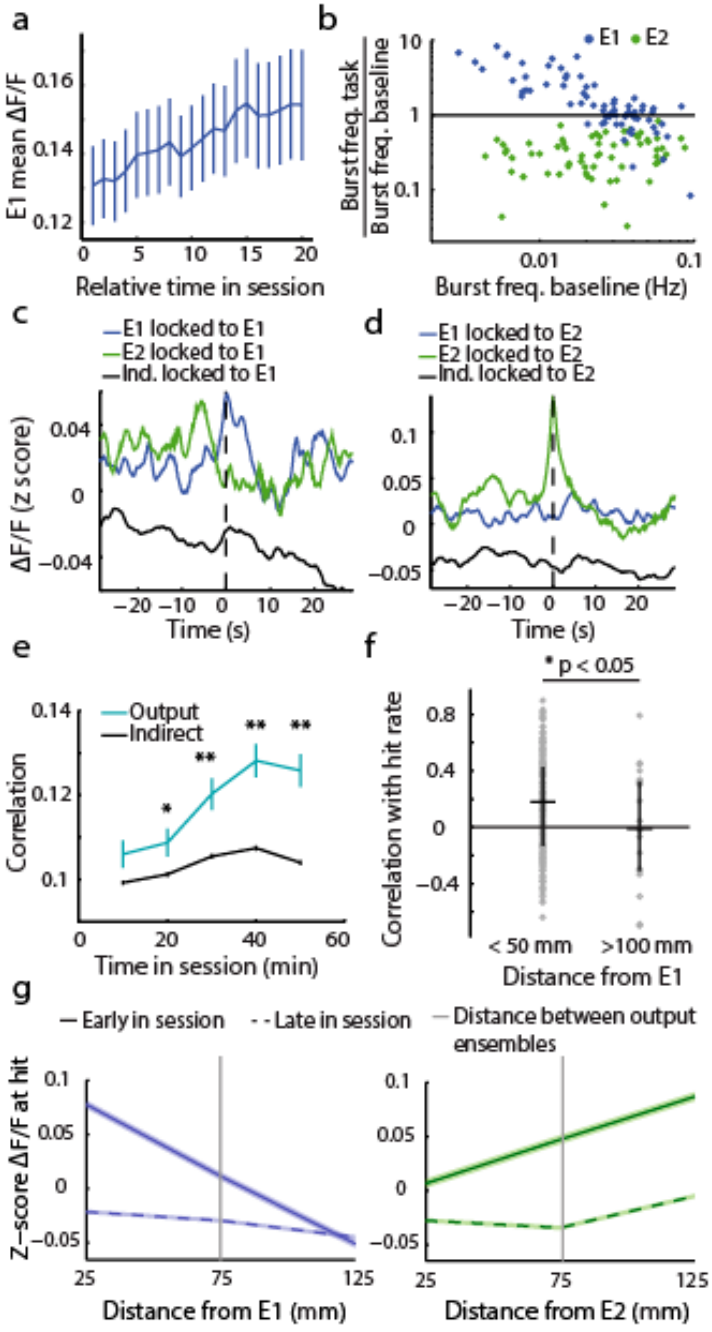

Figure II-4. Local network reorganization accompanies neuroprosthetic learning. a. Mean fluorescence increases in E1 cells over the course of a session. **b.** E1 cells with low baseline activity increase their activity more during the task than cells with high baseline activity. E2 cells suppress their activity evenly. Note logarithmic scale. **c.** Activity in E1, E2 and indirect cells time-locked to large events in E1 cells. **d.** Activity in E1, E2 and indirect cells time-locked to large events in E2 cells. **e.** Correlations increase between output cells (cyan) during the session, with no similar increase in correlations between indirect cells (black). **f.** Indirect cells near output cells have more task-related activity than those far from output cells. Circles are individual cells, bars indicate s.e.m. **g.** Early in a session (solid lines), target-related modulations in indirect cells

decrease with distance from E1 cells (blue) and increase with distance from E2 cells (green). Later in the session (dashed lines) there are no significant modulations in indirect cells, regardless of distance from output cells. Shaded areas represent 95% confidence intervals.

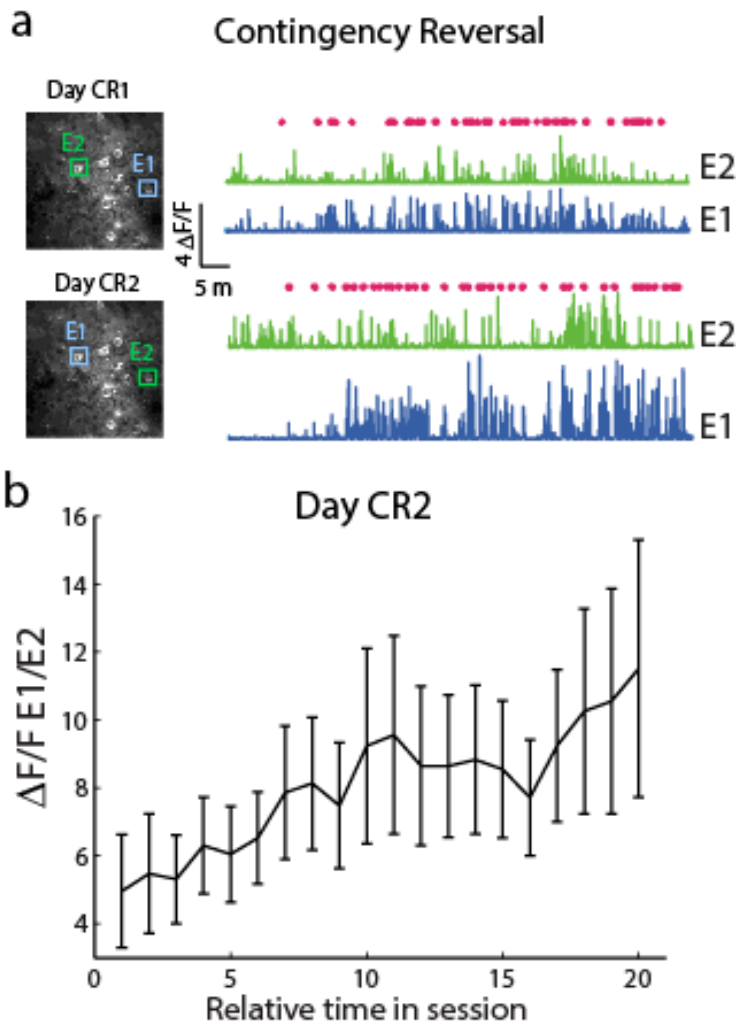

Figure II-5. Fluorescence modulations during contingency reversal experiments. a. When the identity of output cells is changed from day 1 to day 2, animals learn to reverse the activity patterns of their output neurons. **b.** DF/F E1/E2 ratio increases over the course of training on day CR2 (N=3 mice, 20 time points, R2=0.832, p=0.02, t (18)=13.32). Error bars s.e.m.

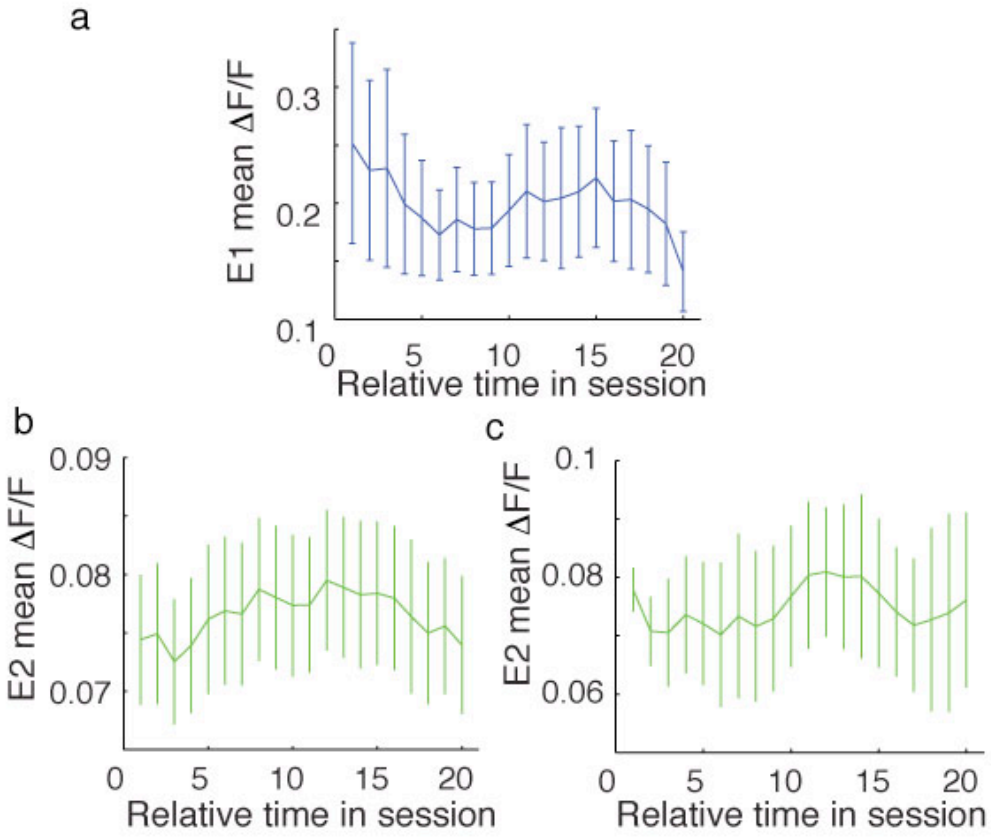

Figure II-6. Fluorescence modulations during contingency degradation experiments a. Mean fluorescence decreases in E1 cells during the contingency degradation manipulation. **b.** Mean DF/F is unchanged in E2 cells over the course of a normal training session (N=5 mice, 20 time points, p=0.234,t (18)=1.23). **c**. Mean DF/F is unchanged in E2 cells during the contingency degradation manipulation (N=5 mice, 20 time points, p=0.13,t (18)=-1.58). Together, these results suggest that animals primarily perform the task by modulating mean activity in E1 cells and do not coarsely modulate the mean activity of E2 cells. Error bars in all panels represent mean +/- SEM.

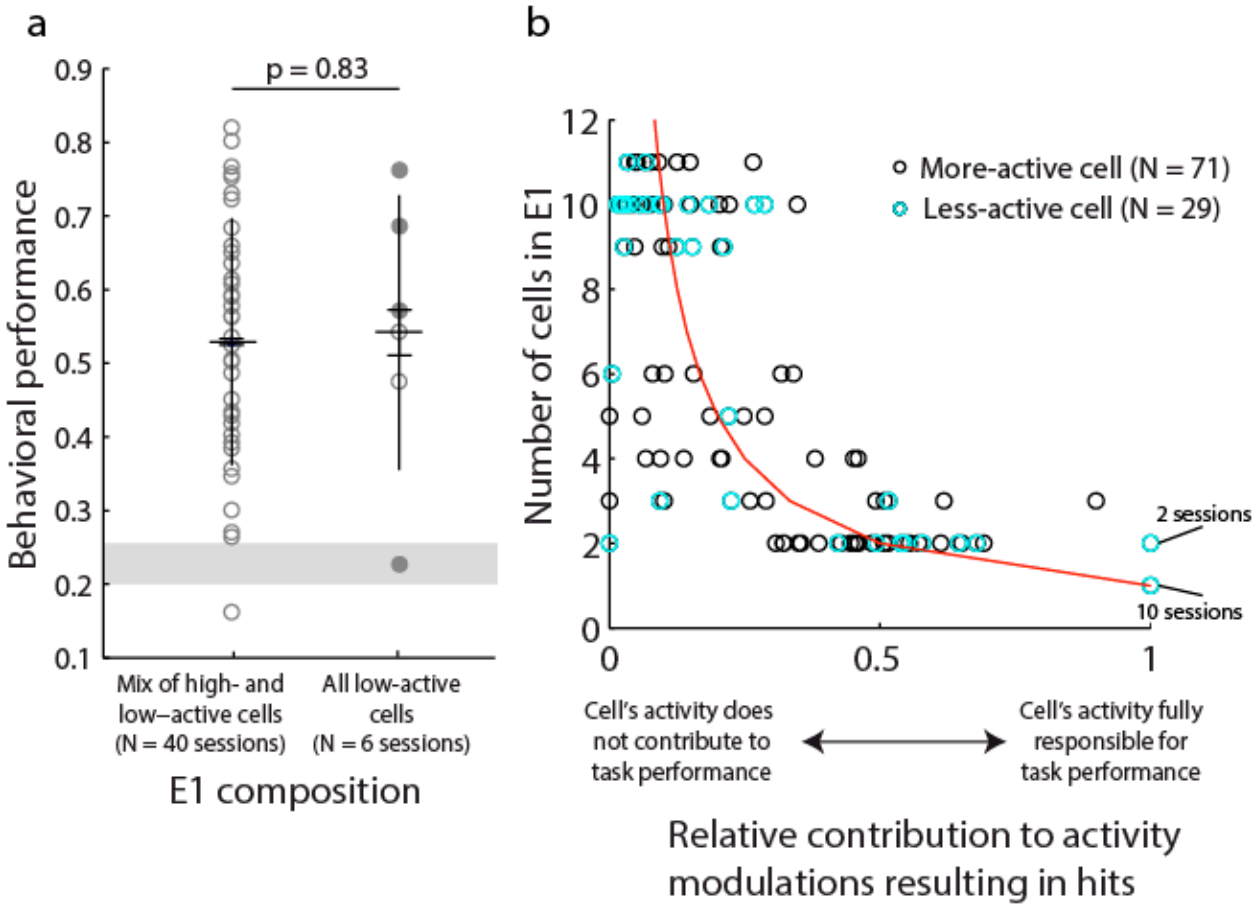

Figure II-7. Performance does not depend on baseline activity in E1 cells.

a. Behavioral performance plotted against the makeup of E1. In 40 sessions, E1 was composed of a mix of more- and less-active cells (defined as cells in the lowest quintile of spontaneous activity rates). In 6 training sessions, E1 was solely comprised of low-active cells, and in 4 cases all cells in E1 had zero baseline activity (filled circles); in three cases the animal still performed the task above chance. Performance in both conditions was significantly better than chance (t-test, high- and low-active ensembles, p=2.2e-15, t (38)=11.69; low-active ensembles, p=0.02, t (5)=3.7). **b**. Analysis of the contribution of individual E1 cells to learned modulation of E1 ensemble activity. Fluorescence modulations around hits were calculated for each E1 cell, and normalized to the sum of modulations in the entire ensemble. Each cell's relative contribution to these modulations was then averaged over the entire training session, and plotted against the number of cells in the E1 ensemble. A bimodal distribution of contributions around 0 and 1 would suggest the task were carried solely by one cell in an ensemble. If all cells contributed equally, the distribution would peak around 1/N (red curve), where N = number of cells in the ensemble. The animals appear to use a combination of both strategies. Less-active neurons (in blue) contributed to hits in a manner indistinguishable from more-active neurons.

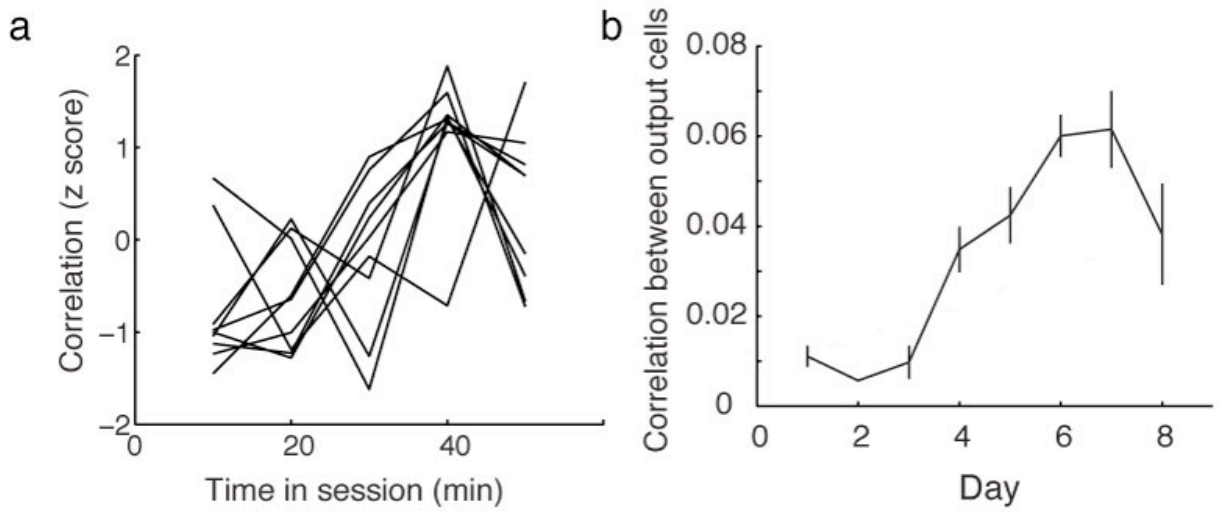

Figure II-8. Correlations between output cells increase over the course of a session and the course of training. A. Z-scored correlations between output cells over the course of a behavioral session shown separately for each animal tested. All animals exhibit the same increasing trend that was seen in the mean. **b.** Correlations between output cells increase across days of training on the task (N=8 days, 10 mice, p=0.011, t (6)=3.59). The composition of ensembles varied across days, so this may reflect meta-learning rather than an increase in correlations between individual cells.

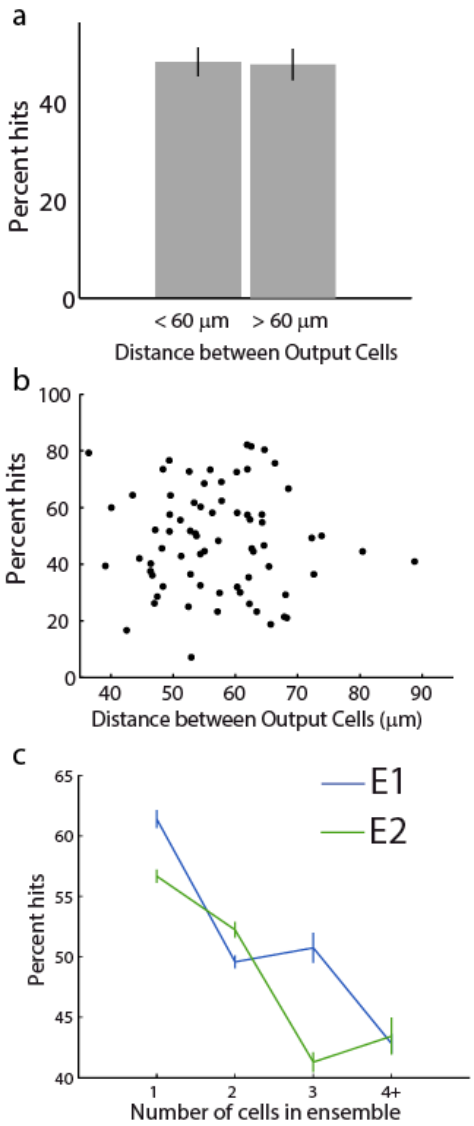

Figure II-9. Performance is not affected by the distance between output cells, but does depend on the number of cells in an ensemble. a. There is no significant difference in performance during sessions in which the output cell ensembles were separated by less than 60 µm and those in which the ensembles were separated by more than 60 µm. Error bars denote s.e.m. **b.** Scatter of performance vs. distance between E1 and E2. **c.** Average performance vs. number of cells in E1 (blue) and E2 (green). Error bars denote s.e.m.

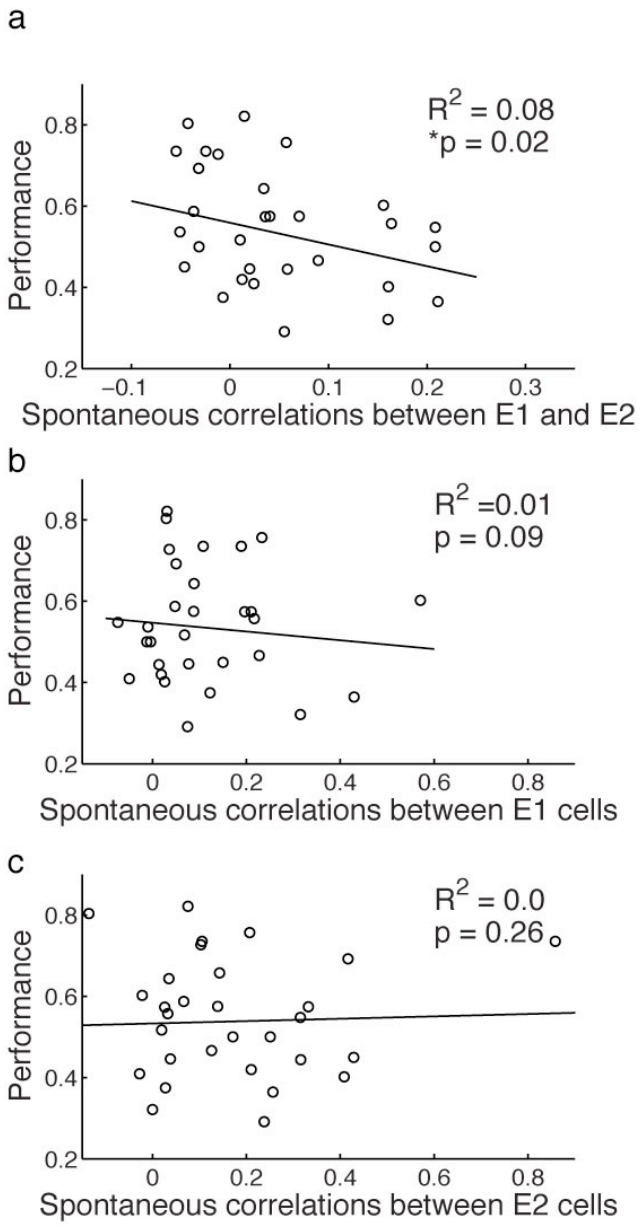

Figure II-10. Performance is affected by baseline correlations between ensembles. a. Animals performed worse when E1 and E2 cells were more spontaneously correlated than when they were less correlated. (N=31 sessions, 10 mice). This effect was not evident **b.** within E1 or **c.** within E2.

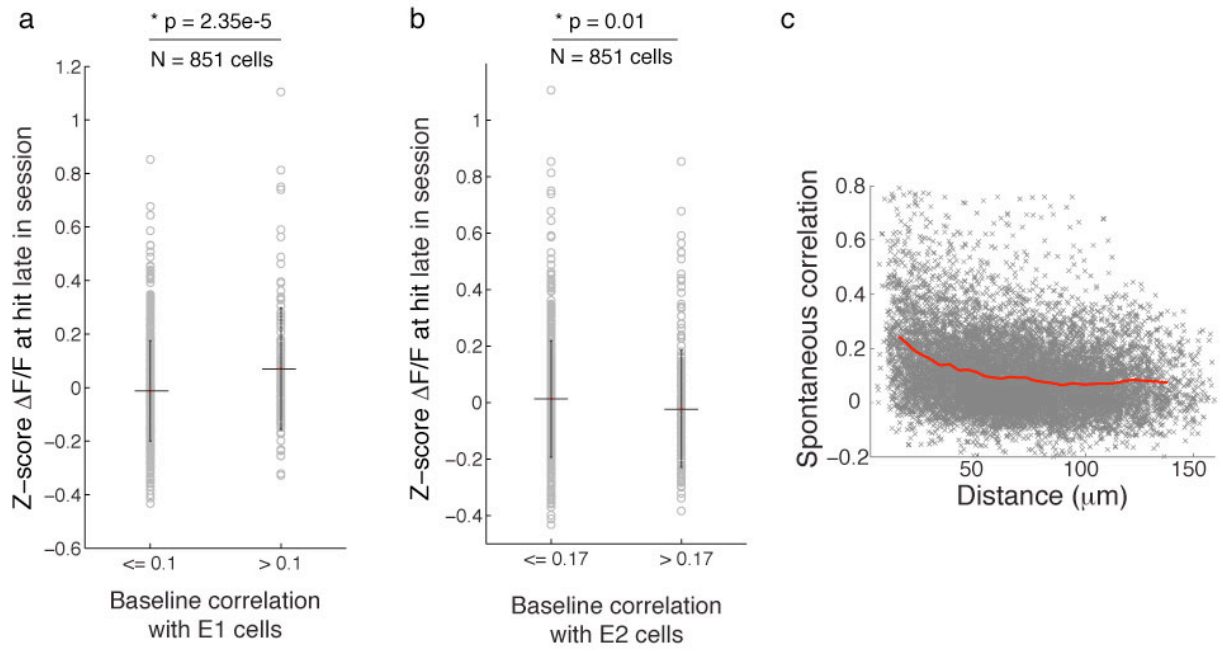

Figure II-11. Indirect cells initially more correlated with output cells maintain output cell-like activity late in session a. Indirect cells that were more spontaneously correlated with E1 cells (highest quintile of spontaneous correlations, >0.1) increase activity during task performance more than cells that were initially weakly, or anti-, correlated (t-test, p = 2.35e-5, t (849)=4.26). Horizontal bar indicates mean, vertical bar indicates standard deviation. **b.** Indirect cells that were more spontaneously correlated with E2 cells (highest quintile of spontaneous correlations, >0.17) show reduced activity during task perfomance compared with less-correlated cells (t-test, p = 0.01, t (849)=-2.6). Horizontal bar indicates mean, vertical bar indicates standard deviation. **c.** Spontaneous correlations between L2/3 neurons in mice fall off rapidly with short distances (binned mean shown in red, S1 and M1 data pooled).

REFERENCES

Andermann, M.L., and Moore, C.I. (2006). A somatotopic map of vibrissa motion direction within a barrel column. *9*, 543–551.

Armstrong-James, M., and Fox, K. (1987). Spatiotemporal convergence and divergence in the rat S1 “barrel” cortex. *263*, 265–281.

Bandyopadhyay, S., Shamma, S.A., and Kanold, P.O. (2010). Dichotomy of functional organization in the mouse auditory cortex. Nature Publishing Group *13*, 361–368.

Barth, A.L., and Poulet, J.F.A. (2012). Experimental evidence for sparse firing in the neocortex. Trends in Neurosciences *35*, 345–355.

Ben Engelhard, Ozeri, N., Israel, Z., Bergman, H., and Vaadia, E. (2013). Inducing Gamma Oscillations and Precise Spike Synchrony by Operant Conditioning via Brain-Machine Interface. Neuron *77*, 361–375.

Benedetti, B.L., Takashima, Y., Wen, J.A., Urban-Ciecko, J., and Barth, A.L. (2012). Differential Wiring of Layer 2/3 Neurons Drives Sparse and Reliable Firing During Neocortical Development. Cerebral Cortex.

Bonin, V., Histed, M.H., Yurgenson, S., and Reid, R.C. (2011). Local diversity and fine-scale organization of receptive fields in mouse visual cortex. *31*, 18506–18521.

Brecht, M. (2003). Dynamic receptive fields of reconstructed pyramidal cells in layers 3 and 2 of rat somatosensory barrel cortex. The Journal of Physiology *553*, 243–265.

Bureau, I., Saint Paul, von, F., and Svoboda, K. (2006). Interdigitated paralemniscal and lemniscal pathways in the mouse barrel cortex. *4*, e382.

Buzsaki, G., and Mizuseki, K. (2014). The log-dynamic brain: how skewed distributions affect network operations. Nat Rev Neurosci *15*, 264–278.

Carmena, J.M., Lebedev, M.A., Crist, R.E., O'Doherty, J.E., Santucci, D.M., Dimitrov, D.F., Patil, P.G., Henriquez, C.S., and Nicolelis, M.A.L. (2003). Learning to Control a Brain–Machine Interface for Reaching and Grasping by Primates. PLoS Biology *1*, e42.

Ch'ng, Y.H. (2010). Cellular imaging of visual cortex reveals the spatial and functional organization of spontaneous activity. Frontiers in Integrative Neuroscience.

Chen, J.L., Carta, S., Soldado-Magraner, J., Schneider, B.L., and Helmchen, F. (2013a). Behaviour-dependent recruitment of long-range projection neurons in somatosensory cortex. Nature *499*, 336–340.

Chen, T.-W., Wardill, T.J., Sun, Y., Pulver, S.R., Renninger, S.L., Baohan, A., Schreiter, E.R., Kerr, R.A., Orger, M.B., Jayaraman, V., et al. (2013). Ultrasensitive fluorescent proteins for imaging neuronal activity. Nature *499*, 295–300.

Crochet, S., Poulet, J.F.A., Kremer, Y., and Petersen, C.C.H. (2011). Synaptic Mechanisms Underlying Sparse Coding of Active Touch. Neuron *69*, 1160–1175.

de Kock, C.P.J., Bruno, R.M., Spors, H., and Sakmann, B. (2007). Layer- and cell-type-specific suprathreshold stimulus representation in rat primary somatosensory cortex. The Journal of Physiology *581*, 139–154.

de Kock, C.P.J., de Kock, C.P.J., Sakmann, B., and Sakmann, B. (2009). Spiking in primary somatosensory cortex during natural whisking in awake head-restrained rats is cell-type specific. *106*, 16446–16450.

Denk, W., Strickler, J.H., Webb, W.W. (1990). Two-photon laser scanning fluorescence microscopy. Science *248*, 73-76.

Dias-Ferreira, E., Sousa, J.C., Melo, I., Morgado, P., Mesquita, A.R., Cerqueira, J.J., Costa, R.M., and Sousa, N. (2009). Chronic Stress Causes Frontostriatal Reorganization and Affects Decision-Making. Science *325*, 621–625.

Drew, P.J., and Feldman, D.E. (2009). Intrinsic Signal Imaging of Deprivation-Induced Contraction of Whisker Representations in Rat Somatosensory Cortex. Cerebral Cortex *19*, 331–348.

Elstrott, J., Clancy, K., Jafri, H., Akimenko, I., and Feldman, D.E. (2014). Cellular mechanisms for response heterogeneity among L2/3 pyramidal cells in whisker somatosensory cortex. Journal of Neurophysiology.

Estebanez, L., Boustani, El, S., Destexhe, A., and Shulz, D.E. (2012). Correlated input reveals coexisting coding schemes in a sensory cortex. *15*, 1691–1699.

Feldman, D.E. (2005). Map Plasticity in Somatosensory Cortex. Science *310*, 810–815.

Ganguly, K., Dimitrov, D.F., Wallis, J.D., and Carmena, J.M. (2011). Reversible large-scale modification of cortical networks during neuroprosthetic control. Nature Publishing Group *14*, 662–667.

Garaschuk, O., and Konnerth, A. (2010). In Vivo Two-Photon Calcium Imaging Using Multicell Bolus Loading. Cold Spring Harbor Protocols *2010*, pdb.prot5482–pdb.prot5482.

Gdalyahu, A., Tring, E., Polack, P.-O., Gruver, R., Golshani, P., Fanselow, M.S., Silva, A.J., and Trachtenberg, J.T. (2012). Associative Fear Learning Enhances Sparse Network Coding in Primary Sensory Cortex. Neuron *75*, 121–132.

Gentet, L.J., Avermann, M., Matyas, F., Staiger, J.F., and Petersen, C.C.H. (2010). Membrane Potential Dynamics of GABAergic Neurons in the Barrel Cortex of Behaving Mice. Neuron *65*, 422–435.

Glazewski, S., Giese, K.P., Silva, A., and Fox, K. (2000). The role of alpha-CaMKII autophosphorylation in neocortical experience-dependent plasticity. *3*, 911–918.

Glickfeld, L.L., Andermann, M.L., Bonin, V., and Reid, R.C. (2013). Cortico-cortical projections in mouse visual cortex are functionally target specific. Nature Publishing Group *16*, 219–226.

Gong, S., Doughty, M., Harbaugh, C.R., Cummins, A., Hatten, M.E., Heintz, N., and Gerfen, C.R. (2007). Targeting Cre Recombinase to Specific Neuron Populations with Bacterial Artificial Chromosome Constructs. Journal of Neuroscience *27*, 9817–9823.

Green, A.M., and Kalaska, J.F. (2011). Learning to move machines withthe mind. Trends in Neurosciences *34*, 61–75.

Guizar-Sicairos, M., Thurman, S.T., and Fienup, J.R. (2008). Efficient subpixel image registration algorithms. Optics Letters *33*, 156–158.

Han, Y.K., Köver, H., Insanally, M.N., Semerdjian, J.H., and Bao, S. (2007). Early experience impairs perceptual discrimination. Nature Neuroscience *10*, 1191–1197.

Harris, K.D., and Mrsic-Flogel, T.D. (2013). Cortical connectivity and sensory coding. Nature *503*, 51–58.

Henze, D., Borhegyi, Z., Csicsvari, J., Mamiya, A., Harris, K.D., and Buzsaki, G. (2000). Intracellular Features Predicted by Extracellular Recordings in the Hippocampus In Vivo. Journal of Neurophysiology *84*, 390–400.

Hilario, M.R.F., Clouse, E., Yin, H.H., and Costa, R.M. (2007). Endocannabinoid signaling is critical for habit formation. Frontiers in Integrative Neuroscience *1*, 1–12.

Hochberg, L.R., Bacher, D., Jarosiewicz, B., Masse, N.Y., Simeral, J.D., Vogel, J., Haddadin, S., Liu, J., Cash, S.S., van der Smagt, P., et al. (2012). Reach and grasp by people with tetraplegia using a neurally controlled robotic arm. Nature *485*, 372–375.

Holtmaat, A., de Paola, V., Wilbrecht, L., Trachtenberg, J.T., Svoboda, K., and Portera-Cailliau, C. (2012). Imaging Neocortical Neurons through a Chronic Cranial Window. Cold Spring Harbor Protocols *2012*, 694–701.

Horton, J.C., and Adams, D.L. (2005). The cortical column: a structure without a function. Philosophical Transactions of the Royal Society B *360*, 837–862.

Hromádka, T., Deweese, M.R., and Zador, A.M. (2008). Sparse representation of sounds in the unanesthetized auditory cortex. *6*, e16.

Isely, G., Hillar, C.J., and Sommer, F.T. (2010). Deciphering subsampled data: adaptive compressive sampling as a principle of brain communication.

Jadhav, S.P., Wolfe, J., and Feldman, D.E. (2009). Sparse temporal coding of elementary tactile features during active whisker sensation. Nature Neuroscience *12*, 792–800.

Jarosiewicz, B., Chase, S.M., Fraser, G.W., Velliste, M., Kass, R.E., and Schwartz, A.B. (2008). Functional network reorganization during learning in a brain-computer interface paradigm. Pnas *105*, 19486–19491.

Jarosiewicz, B., Schummers, J., Malik, W.Q., Brown, E.N., and Sur, M. (2012). Functional Biases in Visual Cortex Neurons with Identified Projections to Higher Cortical Targets. Current Biology *22*, 269–277.

Jenkinson, W., and Glickstein, M. (2000). Whiskers, Barrels, and Cortical Efferent Pathways in Gap Crossing by Rats. Journal of Neurophysiology *84*, 1781-1789.

Keller, G.B., Bonhoeffer, T., and Hübener, M. (2012). Sensorimotor Mismatch Signalsin Primary Visual Cortex of the Behaving Mouse. Neuron *74*, 809–815.

Kerr, J.N.D., de Kock, C.P.J., Greenberg, D.S., Bruno, R.M., Sakmann, B., and Helmchen, F. (2007). Spatial Organization of Neuronal Population Responses in Layer 2/3 of Rat Barrel Cortex. Journal of Neuroscience *27*, 13316–13328.

Kerr, J.N.D., Greenberg, D., and Helmchen, F. (2005). Imaging input and output of neocortical networks in vivo. *102*, 14063–14068.

Knutsen, P.M., Pietr, M., and Ahissar, E. (2006). Haptic Object Localization of the Vibrissal System: Behavior and Performance. The Journal of Neuroscience *26*, 8451-8464.

Ko, H., Hofer, S.B., Pichler, B., Buchanan, K.A., Sjöström, P.J., and Mrsic-Flogel, T.D. (2011). Functional specificity of local synaptic connections in neocortical networks. Nature *473*, 87–91.

Komiyama, T., Sato, T.R., O'Connor, D.H., Zhang, Y.-X., Huber, D., Hooks, B.M., Gabitto, M., and Svoboda, K. (2010). Learning-related fine-scale specificity imaged in motor cortex circuits of behaving mice. Nature *464*, 1182–1186.

Koralek, A.C., Costa, R.M., and Carmena, J.M. (2013). Temporally Precise Cell-Specific Coherence Develops in Corticostriatal Networks during Learning. Neuron *79*, 865–872.

Koralek, A.C., Jin, X., Long, J.D., II, Costa, R.M., and Carmena, J.M. (2012). Corticostriatal plasticity is necessary for learning intentional neuroprosthetic skills. Nature *483*, 331–335.

Kremer, Y., Leger, J.F., Goodman, D., Brette, R., and Bourdieu, L. (2011). Late Emergence of the Vibrissa Direction Selectivity Map in the Rat Barrel Cortex. Journal of Neuroscience *31*, 10689–10700.

Lefort, S., Tomm, C., Sarria, J.C.F., and Petersen, C.C.H. (2009). The Excitatory Neuronal Networkof the C2 Barrel Columnin Mouse Primary Somatosensory Cortex. Neuron *61*, 301–316.

Li, L., Bender, K.J., Drew, P.J., Jadhav, S.P., Sylwestrak, E., and Feldman, D.E. (2009). Endocannabinoid signaling is required for development and critical period plasticity of the whisker map in somatosensory cortex. *64*, 537–549.

Li, Y., Lu, H., Cheng, P.-L., Ge, S., Xu, H., Shi, S.-H., and Dan, Y. (2012). Clonally related visual cortical neurons show similar stimulus feature selectivity. Nature *486*, 118–121.

Looger, L.L., and Griesbeck, O. (2012) Genetically encoded neural activity indicators. Current Opinion in Neurobiology 22, 18-23.

Margolis, D.J., Lütcke, H., Schulz, K., Haiss, F., Weber, B., Kügler, S., Hasan, M.T., and Helmchen, F. (2012). Reorganization of cortical population activity imaged throughout long-term sensory deprivation. Nature Neuroscience *15*, 1539–1546.

Morita, T., Kang, H., Wolfe, J., Jadhav, S.P., Feldman, D.E. (2010). Psychometric Curve and Behavioral Strategies for Whisker-Based Texture Discrimination in Rats. PLoS One, 6, e20437.

Mountcastle, V.B. (1997) . The columnar organization of the neocortex. Brain *120*, 701-722.

Movshon, J.A., and Newsome, W.T. (1996). Visual response properties of striate cortical neurons projecting to area MT in macaque monkeys. *16*, 7733–7741.

Nicolelis, M.A.L. (2001). Actions from thoughts. Nature *409*, 403–407.

Niell, C.M., and Stryker, M.P. (2010). Modulation of Visual Responsesby Behavioral State in Mouse Visual Cortex. Neuron *65*, 472–479.

Nussbaumer, J.C., and Van der Loos, H. (1985). An electrophysiological and anatomical study of projections to the mouse cortical barrelfield and its surroundings. *53*, 686–698.

O'Connor, D.H., Clack, N.G., Huber, D., Komiyama, T., Myers, E.W., and Svoboda, K. (2010a). Vibrissa-based object localization in head-fixed mice. *30*, 1947–1967.

O'Connor, D.H., Peron, S.P., Huber, D., and Svoboda, K. (2010b). Neural Activity in Barrel Cortex Underlying Vibrissa-Based Object Localization in Mice. Neuron *67*, 1048–1061.

Ohki, K., Chung, S., Ch'ng, Y.H., Kara, P., and Reid, R.C. (2005). Functional imaging with cellular resolution reveals precise micro-architecture in visual cortex. *433*, 597–603.

Ohki, K., Chung, S., Kara, P., Hübener, M., Bonhoeffer, T., and Reid, R.C. (2006). Highly ordered arrangement of single neurons in orientation pinwheels. *442*, 925–928.

Olshausen, B., and FIELD, D. (2004). Sparse coding of sensory inputs. Current Opinion in

Neurobiology *14*, 481–487.

Olshausen, B.A., and Field, D.J. (1996). Emergence of simple-cell receptive field properties by learning a sparse code for natural images. Nature *381*, 607–609.

Panzeri, S., Petroni, F., Petersen, R.S., and Diamond, M.E. (2003). Decoding neuronal population activity in rat somatosensory cortex: role of columnar organization. *13*, 45–52.

Perez-Orive, J. (2002). Oscillations and Sparsening of Odor Representations in the Mushroom Body. Science *297*, 359–365.

Petreanu, L., Gutnisky, D.A., Huber, D., Xu, N.-L., O'Connor, D.H., Tian, L., Looger, L., and Svoboda, K. (2012). Activity in motor–sensory projections reveals distributed coding in somatosensation. Nature *489*, 299–303.

Pologruto, T.A., Sabatini, B.L., and Svoboda, K. (2003). ScanImage: Flexible software for operating laser scanning microscopes. BioMed Eng OnLine *2*, 13.

Poo, C., and Isaacson, J.S. (2009). Odor representations in olfactory cortex: "sparse" coding, global inhibition, and oscillations. *62*, 850–861.

Robinson, D.A. (1968). The Electrical Properties of Metal Microelectrodes. Proceedings of the IEEE *56*, 1065–1071.

Rolls, E.T., and Tovee, M.J. (1995). Sparseness of the Neuronal Representation of Stimuli in the Primate Temporal Visual Cortex. Journal of Neurophysiology *73*, 713–726.

Rothschild, G., Nelken, I., and Mizrahi, A. (2010). Functional organization and population dynamics in the mouse primary auditory cortex. Nature Publishing Group *13*, 353–360.

Sachidhanandam, S., Sreenivasan, V., Kyriakatos, A., Kremer, Y., and Petersen, C.C.H. (2013). Membrane potential correlates of sensory perception in mouse barrel cortex. Nature Publishing Group *16*, 1671–1677.

Sakata, S., and Harris, K.D. (2009). Laminar Structure of Spontaneous and Sensory-Evoked Population Activityin Auditory Cortex. Neuron *64*, 404–418.

Saleem, A.B., Ayaz, A., Jeffery, K.J., Harris, K.D., and Carandini, M. (2013). Integration of visual motion and locomotion in mouse visual cortex. Nature Publishing Group *16*, 1864–1869.

Sato, T.R., and Svoboda, K. (2010). The Functional Properties of Barrel Cortex Neurons Projecting to the Primary Motor Cortex. Journal of Neuroscience *30*, 4256–4260.

Sato, T.R., Gray, N.W., Mainen, Z.F., and Svoboda, K. (2007). The Functional Microarchitecture of the Mouse Barrel Cortex. PLoS Biology *5*, e189.

Shepherd, G.M.G., and Svoboda, K. (2005). Laminar and columnar organization of ascending excitatory projections to layer 2/3 pyramidal neurons in rat barrel cortex. *25*, 5670–5679.

Shoham, S., O'Connor, D.H., and Segev, R. (2006). How silent is the brain: is there a “dark matter” problem in neuroscience? J Comp Physiol A *192*, 777–784.

Stettler, D.D., and Axel, R. (2009). Representations of odor in the piriform cortex. *63*, 854–864.

Stosiek, C., Garaschuk, O., Holthoff, K., and Konnerth, A. (2003). In vivo two-photon calcium imaging of neuronal networks. Pnas *100*, 7319–7324.

Suter, B. (2010). Ephus: multipurpose data acquisition software for neuroscience experiments. Front. Neural Circuits *4*.

Tamamaki, N., Yanagawa, Y., Tomioka, R., Miyazaki, J.-I., Obata, K., and Kaneko, T. (2003). Green fluorescent protein expression and colocalization with calretinin, parvalbumin, and somatostatin in the GAD67-GFP knock-in mouse. The Journal of Comparative Neurology *467*, 60–79.

Thévenaz, P.P., Ruttimann, U.E.U., and Unser, M.M. (1998). A pyramid approach to subpixel registration based on intensity. Image Processing, IEEE Transactions on *7*, 27–41.

Tian, L., Hires, A., Mao, T., Huber, D., Chiappe, M. E., Chalasani, S. H., Petreanu, L., Akerboom, J., McKinney, S.A., Schreiter, E.R., Bargmann, C.I., Jayaraman, V., Svoboda, K., Looger, L. (2009). Imaging neural activity in worms, flies and mice with improved GCaMP calcium indicators. Nature Methods *6*, 875-881.

Vinje, W.E., and Gallant, J.L. (2000). Sparse coding and decorrelation in primary visual cortex during natural vision. Science *287*, 1273–1276.

Vogelstein, J.T., Packer, A.M., Machado, T.A., Sippy, T., Babadi, B., Yuste, R., and Paninski, L. (2010). Fast Nonnegative Deconvolution for Spike Train Inference From Population Calcium Imaging. Journal of Neurophysiology *104*, 3691–3704.

Winkowski, D.E., and Kanold, P.O. (2013). Laminar Transformation of Frequency Organization in Auditory Cortex. Journal of Neuroscience *33*, 1498–1508.

Wodlinger, B., Downey, J.E., Wang, W., Tyler-Kabara, E.C., Weber, D.J., McMorland, A.J.C., Velliste, M., Collinger, J.L., Boninger, M.L., and Schwartz, A.B. (2013). High-performance neuroprosthetic control by an individualwith tetraplegia. The Lancet *381*, 557–564.

Wolfe, J., Houweling, A.R., and Brecht, M. (2010). Sparse and powerful cortical spikes. Current Opinion in Neurobiology *20*, 306–312.

Yaka, R., Yinon, U., and Wollberg, Z. (1999). Auditory activation of cortical visual areas in cats after early visual deprivation. European Journal of Neuroscience *11*, 1301–1312.

Yamashita, T., Pala, A., Pedrido, L., Kremer, Y., Welker, E., and Petersen, C.C.H. (2013). Membrane potential dynamics of neocortical projection neurons driving target-specific signals. *80*, 1477–1490.

Yassin, L., Benedetti, B.L., Jouhanneau, J.-S., Wen, J.A., Poulet, J.F.A., and Barth, A.L. (2010). An Embedded Subnetwork of Highly Active Neurons in the Neocortex. Neuron *68*, 1043–1050.

Zhou, M., Liang, F., Xiong, X.R., Li, L., Li, H., Xiao, Z., Tao, H.W., and Zhang, L.I. (2014). Scaling down of balanced excitation and inhibition by active behavioral states in auditory cortex. Nature Publishing Group.